

Article

Pan-KRAS inhibitor disables oncogenic signalling and tumour growth

<https://doi.org/10.1038/s41586-023-06123-3>

Received: 8 September 2022

Accepted: 24 April 2023

Published online: 31 May 2023

Open access

 Check for updates

Dongsung Kim^{1,2,6}, Lorenz Herdeis^{3,6}, Dorothea Rudolph^{3,6}, Yulei Zhao¹, Jark Böttcher³, Alberto Vides¹, Carlos I. Ayala-Santos¹, Yasin Pourfarjam¹, Antonio Cuevas-Navarro¹, Jenny Y. Xue¹, Andreas Mantoulidis³, Joachim Bröker³, Tobias Wunberg³, Otmar Schaar³, Johannes Popow³, Bernhard Wolkerstorfer³, Katrin Gabriele Kropatsch³, Rui Qu⁴, Elisa de Stanchina⁴, Ben Sang¹, Chuanchuan Li¹, Darryl B. McConnell^{3,7}, Norbert Kraut^{3,7} & Piro Lito^{1,2,5,7}✉



KRAS is one of the most commonly mutated proteins in cancer, and efforts to directly inhibit its function have been continuing for decades. The most successful of these has been the development of covalent allele-specific inhibitors that trap KRAS G12C in its inactive conformation and suppress tumour growth in patients^{1–7}. Whether inactive-state selective inhibition can be used to therapeutically target non-G12C KRAS mutants remains under investigation. Here we report the discovery and characterization of a non-covalent inhibitor that binds preferentially and with high affinity to the inactive state of KRAS while sparing NRAS and HRAS. Although limited to only a few amino acids, the evolutionary divergence in the GTPase domain of RAS isoforms was sufficient to impart orthosteric and allosteric constraints for KRAS selectivity. The inhibitor blocked nucleotide exchange to prevent the activation of wild-type KRAS and a broad range of KRAS mutants, including G12A/C/D/F/V/S, G13C/D, V14I, L19F, Q22K, D33E, Q61H, K117N and A146V/T. Inhibition of downstream signalling and proliferation was restricted to cancer cells harbouring mutant KRAS, and drug treatment suppressed KRAS mutant tumour growth in mice, without having a detrimental effect on animal weight. Our study suggests that most KRAS oncoproteins cycle between an active state and an inactive state in cancer cells and are dependent on nucleotide exchange for activation. Pan-KRAS inhibitors, such as the one described here, have broad therapeutic implications and merit clinical investigation in patients with KRAS-driven cancers.

KRAS mutations are among the most frequent gain-of-function alterations found in patients with cancer and their therapeutic targeting has long been a key objective in precision oncology^{8–12}. The KRAS GTPase cycles between an active (GTP-bound) and an inactive (GDP-bound) state. GTP hydrolysis is enhanced by GTPase-activating proteins¹³, whereas GDP to GTP exchange is enhanced by guanine nucleotide exchange factors¹⁴. Allele-specific inhibitors, which bind covalently to KRAS G12C and trap it in an inactive state^{2,15}, have demonstrated clinical benefits in patients with lung cancer^{5–7}. These drugs, however, require a reactive cysteine residue for inhibition and cannot be used against non-G12C mutants, which constitute most KRAS alterations in cancer. As such, efforts to identify therapeutics that enable broad inhibition of KRAS mutants are continuing. Moreover, the most prevalent of non-G12C KRAS mutants found in cancer are thought to be deficient in GAP-assisted GTP hydrolysis^{16–21} and exist in a non-excitatory or constitutively active state. As such, it is not clear whether the inactive-state selective trapping mechanism afforded by covalent G12Ci (refs. 2,22,23), will work against non-G12C mutants.

To address these issues, we set out to develop small molecule pan-KRAS inhibitors that do not discriminate between KRAS mutants. We began by removing the covalent warhead from the G12C-selective inhibitor BI-0474 (Fig. 1a) and applied structure-based design optimizations to obtain a potent non-covalent inhibitory activity. The latter was assayed by determining the effect on the proliferation of isogenic BaF3 cells engineered to express G12C, G12D or G12V mutant KRAS (Fig. 1b and Extended Data Fig. 1a; a broader analysis across other KRAS mutants is shown below). Although the removal of the covalent warhead (precursor 1) greatly reduced the potency of G12C inhibition, we were surprised to find that the warhead-free scaffold indiscriminately inhibited proliferation driven by the noted KRAS variants, albeit with a low potency (half-maximum inhibitory concentration (IC_{50}) $\geq 1 \mu\text{M}$). The crystal structure of precursor 1 in complex with wild-type (WT) KRAS (Extended Data Fig. 1b) showed that the piperazine moiety was suboptimally positioned between the carboxylates of E62 in the Switch II motif and D92 in the $\alpha 3$ helix of KRAS. Furthermore, we observed a highly coordinated water molecule near the C5 atom of the pyridine

¹Human Oncology and Pathogenesis Program, Memorial Sloan Kettering Cancer Center, New York, NY, USA. ²Department of Medicine, Memorial Sloan Kettering Cancer Center, New York, NY, USA. ³Boehringer Ingelheim, Vienna, Austria. ⁴Antitumor Assessment Core Facility, Memorial Sloan Kettering Cancer Center, New York, NY, USA. ⁵Department of Medicine, Weill Cornell Medical College, New York, NY, USA. ⁶These authors contributed equally: Dongsung Kim, Lorenz Herdeis, Dorothea Rudolph. ⁷These authors jointly supervised this work: Darryl B. McConnell, Norbert Kraut, Piro Lito.  e-mail: litop@mskcc.org

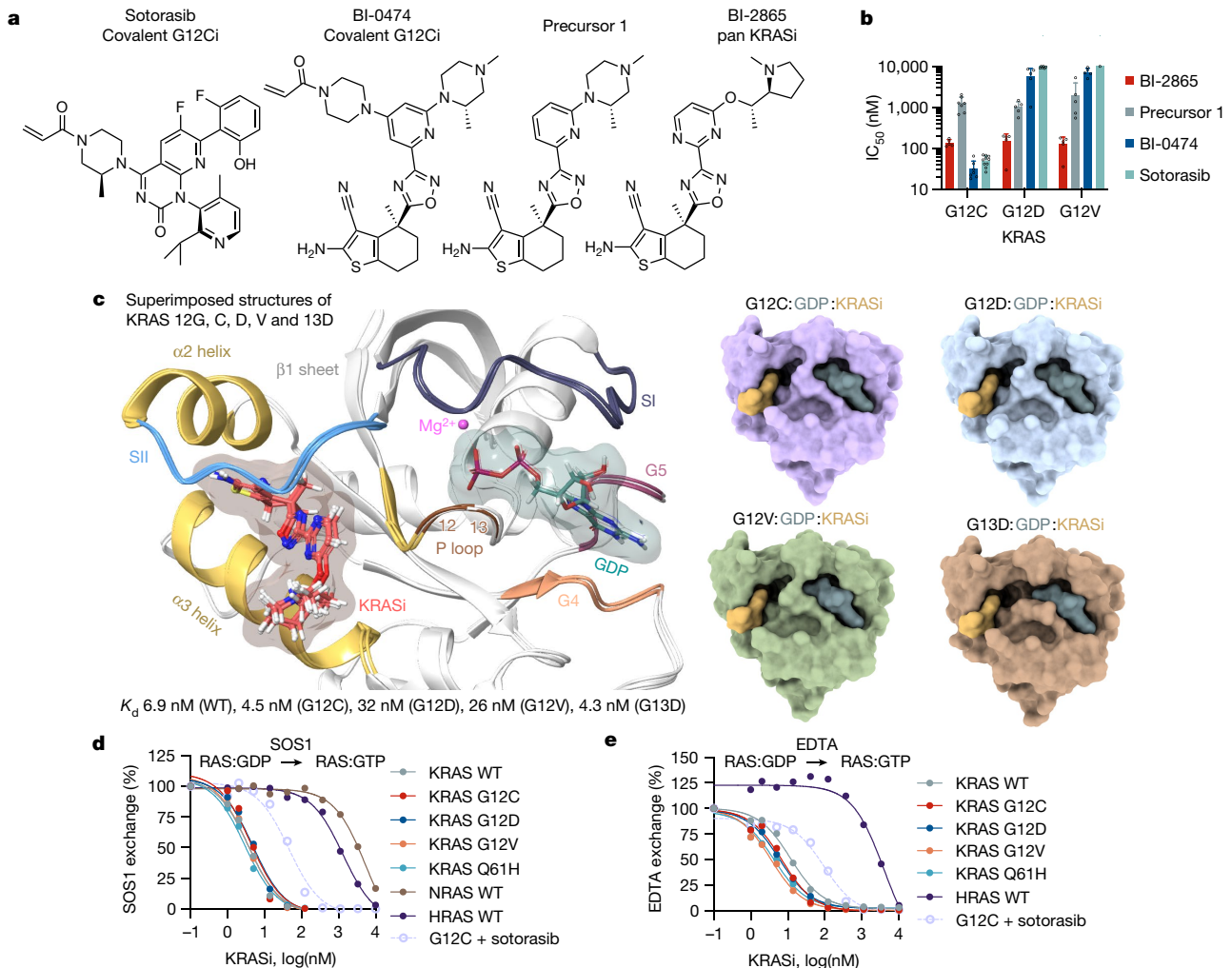


Fig. 1 | Identification of a non-covalent inhibitor that inactivates common cancer-causing KRAS mutants. **a**, Chemical structures of the indicated compounds. **b**, Isogenic BaF3 cells expressing the indicated KRAS mutants were treated for 5 days in the absence of IL3 (oncogene dependent growth) to determine the effect on proliferation (mean \pm s.e.m., $n = 5$, unless otherwise indicated, n denotes biological replicates). **c**, Cocrystal structures of drug-bound WT, G12C, G12D, G12V and G13D mutant KRAS. **d,e**, The effect of KRASi treatment on nucleotide exchange stimulated either by SOS1 (**d**) or EDTA (**e**). The reaction of KRAS G12C with the covalent inhibitor sotorasib is shown for comparison. A representative of two independent repeats is shown in **d** and **e**.

indicated, n denotes biological replicates). **c**, Cocrystal structures of drug-bound WT, G12C, G12D, G12V and G13D mutant KRAS. **d,e**, The effect of KRASi treatment on nucleotide exchange stimulated either by SOS1 (**d**) or EDTA (**e**). The reaction of KRAS G12C with the covalent inhibitor sotorasib is shown for comparison. A representative of two independent repeats is shown in **d** and **e**.

ring (3.6 Å). We thus proposed that the potency of precursor 1 could be enhanced by improving its interaction with E62 and by introducing an acceptor functionality at C5. Extensive optimization led to BI-2865, a derivative with a prolinol substituent and a pyrimidine linker, which enabled a direct ionic interaction with E62, as well as a water-mediated hydrogen bond network with the side chain of R68 and the main chain carbonyl of Q61 (Extended Data Fig. 1c and below). As a result, BI-2865 inhibited the proliferation of isogenic G12C, G12D or G12V mutant KRAS expressing BaF3 cells more potently than precursor 1 with a mean IC_{50} of roughly 140 nM (Fig. 1b). In KRAS G12C-expressing BaF3 cells, the effect of BI-2865, a compound lacking the Michael acceptor needed for covalent bonding, was comparable to that of covalent KRAS G12C inhibitors BI-0474 and sotorasib. Little if any antiproliferative effect was observed when BaF3 cells were treated in the presence of IL3, a condition that stimulates oncogene-independent growth in this system (Extended Data Fig. 1a). Encouraged by these observations we decided to study further the effects of BI-2865 and its related compounds, referring to them as pan-KRASi inhibitors or KRASi.

We established high-resolution cocrystal structures (1.0–1.1 Å) of the pan-KRASi (BI-2865) in complex with several KRAS variants (Fig. 1c, Extended Data Fig. 1d and Extended Data Table 1). These showed a

conserved binding pocket across variants (Fig. 1c and Extended Data Fig. 1c) defined by the α_2 and α_3 helices, the distal portion of the β 1 sheet and the distal portion of the Switch II motif in KRAS (Fig. 1c). A part of the KRASi pocket overlapped with that occupied by covalent G12C inhibitors, such as sotorasib and adagrasib, with the notable difference that the pan-KRASi engaged the pocket without relying on a covalent tether and did not extend in the P-loop channel near the G12 residue (Extended Data Fig. 1c,e).

The inhibitor bound to the GDP-loaded state of WT, G12C, G12D, G12V and G13D KRAS with high affinity (dissociation constant (K_d), 10–40 nM; Fig. 1c), as determined by isothermal titration calorimetry (ITC) (Extended Data Fig. 2a,b). By comparison, the affinity was 60–140 times lower for KRAS variants loaded with the GTP analogue GCP. Selectivity for the inactive state is probably conferred by the conformation of the Switch II motif (including residues Q61 and E62), which partly occupies the drug pocket in the active state conformation of KRAS (Extended Data Fig. 1d). Surface plasmon resonance studies showed reversible drug-binding kinetics with a dissociation rate (k_{off}) ranging between 0.015 and 0.05 s⁻¹ across KRAS variants (Extended Data Fig. 2c).

Drug-bound, GDP-loaded KRAS variants had diminished activation by nucleotide exchange, either when the latter was stimulated by

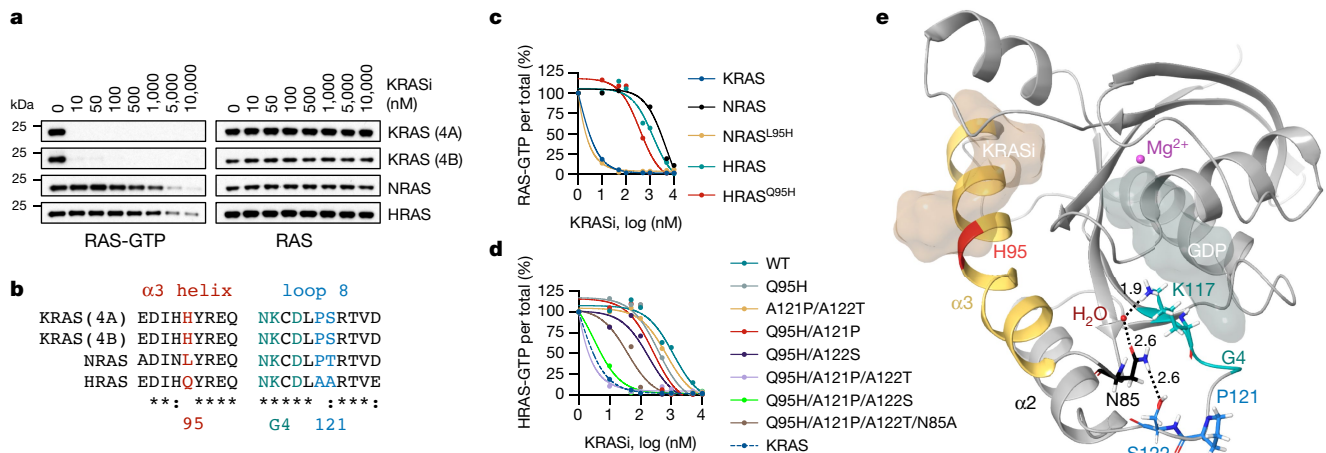


Fig. 2 | Limited evolutionary divergence confers selectivity for KRAS.

a, RASless mouse embryonic fibroblasts expressing the indicated RAS isoforms were treated for 2 h. Cell extracts were subjected to RBD pull down and immunoblotting to determine the amount of active RAS. **b**, Sequence alignment of the G domain of RAS isoforms. **c,d**, Effect of isoform mimetic substitutions on RAS inhibition: RAS-GTP (**c**) and HRAS-GTP (**d**). HEK293 cells

expressing the indicated mutants were treated for 2 h to determine the effect on RAS activation by using RBD pull down, immunoblotting and densitometry. **e**, Cocrystal structure of drug-bound KRAS showing H bonds between S122, N85 and K117 (black dotted lines, distance in Å). A representative of two independent experiments is shown in **a,c** and **d**.

the nucleotide exchange factor SOS1 (Fig. 1d) or by EDTA (Fig. 1e), as well as under intrinsic conditions (Extended Data Fig. 2d). To determine whether low-affinity binding to the active state also inhibited KRAS function, we tested the ability of the inhibitor to displace the RAS-binding domain (RBD) of CRAF from purified GMPPNP-loaded KRAS variants (Extended Data Fig. 2e). The drug prevented effector binding to active KRAS only at high concentrations (mean IC_{50} roughly 5.5 μ M). By contrast, the inhibitory effect of inactive state binding on nucleotide exchange had an IC_{50} of roughly 5 nM. To determine the propensity of the pan-KRASi to target the active state of KRAS mutants in cells, we relied on the transition state mutation A59G, which impairs GTP hydrolysis^{2,24}. Introducing the A59G mutation alongside G12, G13 or Q61 KRAS mutants led to a near complete loss of target inhibition (Extended Data Fig. 2f). The affinity of the A59G mutant for BI-2865 was similar to that of WT KRAS (Extended Data Fig. 2g). In addition, low-affinity drug binding to the active state did not result in enhanced KRAS-GTP hydrolysis (Extended Data Fig. 2h). Together, the data indicate that the drug's inhibitory activity in cells relies predominantly on targeting the inactive or GDP-bound state of KRAS.

The ability of the inhibitor to suppress nucleotide exchange by HRAS or NRAS was several orders of magnitude less than that for KRAS (Fig. 1d,e). To test whether the inhibitor was selective for KRAS in cells, we used 'RASless' murine embryonic fibroblasts (MEFs)²⁵ engineered to express only a single RAS variant (Extended Data Fig. 3a). The drug inhibited the activation of KRAS splice variants 4A and 4B with an IC_{50} of less than 10 nM (Fig. 2a). By comparison the IC_{50} for NRAS and HRAS ranged from 5 to 10 μ M. The pan-KRAS inhibitor suppressed the cellular activation of KRAS with a similar potency to that observed for the covalent KRAS G12C inhibitor sotorasib (Extended Data Figs. 2i and 3b). Together, the data argue that the drug is a pan-KRAS, inactive state selective inhibitor.

Evolutionary divergence in the GTPase (G) domain of RAS isoforms is minimal, with only few non-homologous amino acids present. As such, the ability of the drug to inhibit only a single RAS isoform was not expected a priori. To determine the basis for KRAS selectivity we interrogated amino acid differences between HRAS, NRAS and KRAS (Fig. 2b). Most notable was the substitution of H95 in the α_3 helix of KRAS with L and Q in NRAS and HRAS, respectively. KRAS mimetic substitution at the 95th residue in NRAS (that is, L95H) rendered NRAS almost as

sensitive as KRAS to the effect of the drug (Fig. 2c). By comparison, the Q95H substitution in HRAS had only a partial effect, suggesting that this isoform has further selectivity constraints.

Residues 121 and 122 distinguish HRAS from NRAS and KRAS (Fig. 2b, AA, PT and PS, respectively). Given the divergent effects that KRAS mimetic substitutions at the 95th residue had in NRAS and HRAS, we next tested the possibility that residues 121 and 122 allosterically regulate selective inhibition. As shown in Fig. 2d and Extended Data Fig. 3d, KRAS mimetic substitutions at these positions (that is, A121P and A122S (A121P/A122S)) did not have a sensitizing effect on HRAS. Similarly, the KRAS mimetic substitutions Q95H and A121P (Q95H/A121P) or Q95H and A122S (Q95H/A122S) led to only weak sensitization. By contrast, the triple substitution in HRAS (that is, Q95H, A121P and A122S (Q95H/A121P/A122S)) lead to a similar magnitude of inhibition to that observed in KRAS (Fig. 2d, green line versus rest). As expected, reciprocal H/NRAS mimetic substitutions in KRAS led to attenuated inhibition (Extended Data Fig. 3c). On closer inspection, the cocrystal structure of drug-bound KRAS-GDP suggested contacts between P121, S122 and N85 (Fig. 2e), a residue residing just proximal to the α_3 helix and adjacent to the K117 residue in the G4 motif (see below for why proximity to G4 residues was thought to be important). We thus hypothesized that the allosteric effect of P121 and S122 is modulated at least in part by N85. Indeed, introducing the N85A mutation attenuated the effect of the KRASi on HRAS Q95H/A121P/A122S (Fig. 2d, brown versus green line and Extended Data Fig. 3d). The data therefore indicate that three residues with evolutionary divergence in the G domains of RAS isoforms also impose selectivity constraints on KRAS inhibition. The latter is because of a combination of orthosteric effects by H95 in the α_3 helix and allosteric (or indirect) effects by P121 and S122 in loop 8.

We next sought to determine in an unbiased manner the presence of other amino acids that allosterically modulate inactive state selective KRAS inhibition. To this end, KRAS mutant cells were infected with a doxycycline (dox)-inducible complementary DNA library, encoding for all possible amino acid substitutions in the KRAS G12C backbone, followed by treatment with either dimethylsulfoxide (DMSO) or KRASi for 2 weeks in the presence or absence of dox. Variants with statistically significant changes are shown in Fig. 3a and Extended Data Fig. 4. As expected from the findings above and previous studies with covalent G12C inhibitors^{26,27}, mutations in residues defining the drug-binding

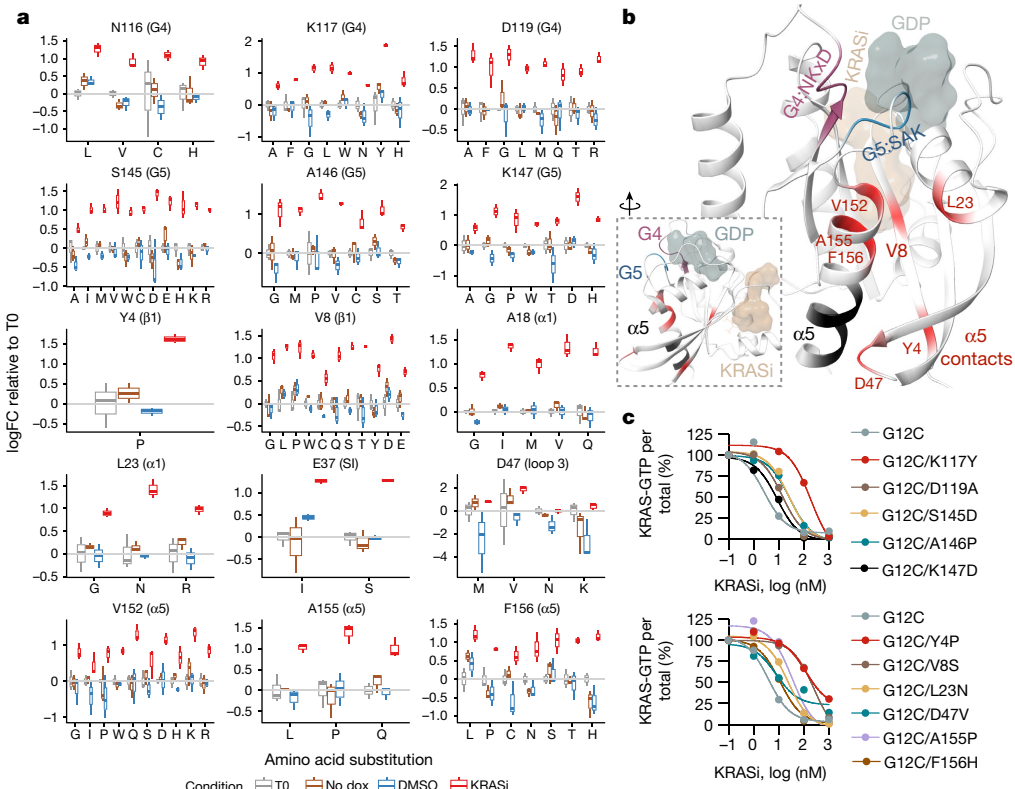


Fig. 3 | Diverse allosteric effects on inactive state selective KRAS inhibition.

a, H358 cells were infected with a dox-inducible saturation mutagenesis library based on a KRAS G12C backbone and treated with either DMSO or KRASi for 2 weeks. The selection of mutations in amino acids far from drug-binding interface are shown (median, interquartile range and Tukey whiskers, $n = 3$). FC, fold change; T0, time 0. **b**, Residues from a were mapped in the cocrystal structure of KRAS G12C with the KRASi inhibitor. Residues involved in α 5

contacts that were not identified in the screen are shown in black. Inset, 90° rotation. **c**, HEK293 cells expressing KRAS with a single G12C mutation or double mutants involving substitutions in the G4 and G5 motifs (top) or α 5 helix contacts (bottom) were treated as shown for 2 h. Cell extracts were subjected to RBD pull down, immunoblotting and densitometry to determine the effect on KRAS-GTP concentrations. A representative of two independent repeats is shown in **c**.

pocket (Extended Data Fig. 4a) led to resistance and were positively selected by treatment. By comparison, mutations in residues at the interface of RAS-GDP and the catalytic subunit of SOS1 were negatively selected by treatment (Extended Data Fig. 4b). The latter suggests that blockade of nucleotide exchange enhances the effect of treatment and is consistent with the inhibitory mechanism of the pan-KRASi (when considering that enhanced nucleotide exchange would diminish the proportion of GDP-bound KRAS—the conformation preferred by the drug). Indeed, pharmacologic inactivation of nucleotide exchange by SOS1 or SHP2 inhibitors led to a more pronounced suppression of KRAS-GTP concentrations by the KRAS inhibitor (Extended Data Fig. 2j).

Mutations in several amino acids residing away from the drug-binding interface were also enriched with treatment (Fig. 3a,b). These included alterations in the G4 (NKxD) and G5 (SAK/L) motifs of the GTPase, as well as several residues that formed contacts with the α 5 helix in the cocrystal structure of drug-bound KRAS G12C (hereafter referred to as α 5 contacts). A similar saturation mutagenesis screen with an inhibitor targeting the GTP-bound state of KRAS G12C (ref. 28) did not identify these variants as being positively selected by treatment (Extended Data Fig. 4c,d), suggesting that they are specifically involved in modulating the inactive state selective inhibition of mutant KRAS. Introducing G4, G5 and α 5 (G4/G5/ α 5) contact mutations alongside G12C led to diminished inhibition of KRAS-GTP concentrations after 2 h of drug treatment (Extended Data Fig. 4e,f and Fig. 3c). The G4/G5/ α 5 double mutants also had a higher baseline KRAS activation than the G12C single mutant (Extended Data Fig. 4e,f; compare lane 1 across rows). Three representative double mutants, G12C/K117Y, G12C/D47V and G12C/F156H,

had a greater ability to undergo nucleotide exchange than KRAS G12C, either in the absence (intrinsic conditions) or the presence of SOS1 or EDTA (Extended Data Fig. 4g). The latter is in agreement with studies showing that naturally occurring mutations in G4 or G5 residues enhance intrinsic or SOS1-mediated nucleotide exchange²⁹. Together, the data indicate that the allosteric effect of G4/G5/ α 5 residues on KRAS inhibition is mediated, at least in part, by modulating the dynamics of the KRAS nucleotide cycle. In agreement, the K117Y mutation reversed the effect that KRAS mimetic substitutions in HRAS had on KRASi treatment (Extended Data Fig. 3d). The latter supports the importance of the P121/S122-N85-K117 interaction network on selective KRAS inhibition.

We next evaluated the ability of the pan-KRASi to suppress KRAS activation and downstream signalling in a panel of 39 cell lines (Fig. 4a), originating from lung, colorectal or pancreatic cancers. Seven cell lines harboured WT KRAS (WT group). Eight cell lines had alterations that activate upstream signalling (upstream activated WT (UAWT) group). Twenty-four cell lines had KRAS mutations (G12C: $n = 4$, G12D: $n = 5$, G12V: $n = 4$, G12S: $n = 1$, G12R: $n = 2$, G13D: $n = 3$, Q61X: $n = 2$, K117N: $n = 1$, A146T: $n = 2$). As expected from the biochemical data, the drug inhibited KRAS activation in both WT and mutant models (Extended Data Fig. 5 and Fig. 4a). The inhibitor also inactivated 18 out of the 24 most common KRAS mutants found in cancer, when the latter were individually expressed in human embryonic kidney 293 (HEK293) cells (Fig. 4b and Extended Data Fig. 6a).

Considering that the KRASi binds to WT and mutant KRAS with a similar affinity (K_d in Fig. 1c), the rate of inhibition may be used to compare the relative propensities of KRAS variants to undergo nucleotide

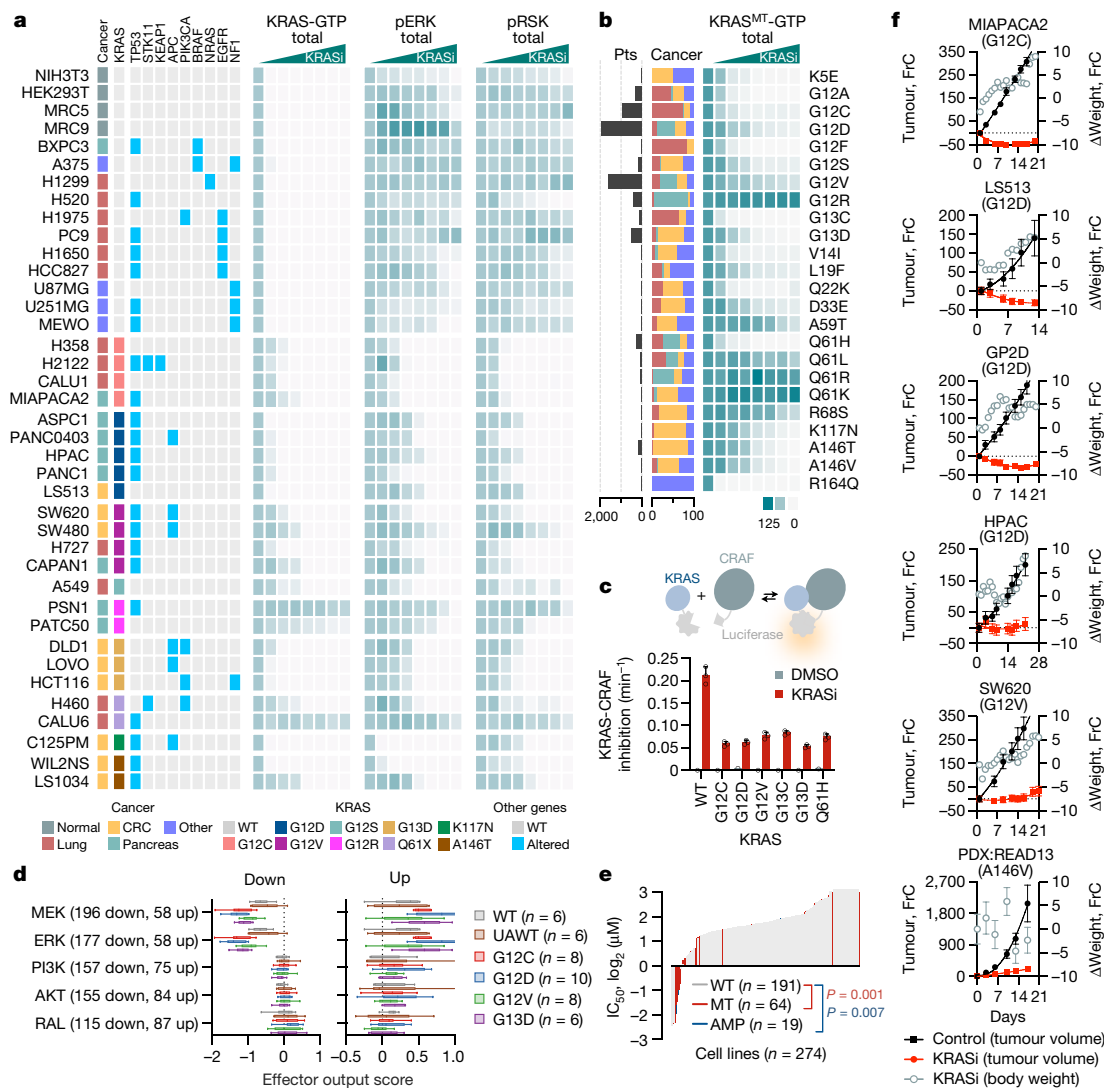


Fig. 4 | Selective inhibition of oncogenic signalling and KRAS-driven tumour growth. **a**, Thirty-nine cell lines were treated for 2 h to determine the effect on KRAS activation and downstream signalling. **b**, HEK293 cells expressing the indicated KRAS mutants were treated as shown and analysed to determine the effect on KRAS activation. The abundance (Pts) and distribution of mutations across cancer types (Cancer, %) are shown. **c**, A split luciferase assay was used to determine the rate constant for the inhibition of the KRAS–CRAF interaction

by treatment in live cells (mean \pm s.e.m., $n = 3$). **d**, Effect of KRASi treatment on the transcriptional output by key RAS effector pathways (median, interquartile range and Tukey whiskers). The number of effector-dependent genes used to calculate the output score is shown in parentheses. **e**, Profiling of IC_{50} in a panel of 274 cell lines. **f**, Mice bearing xenograft models were treated to determine the effect on tumour growth and animal weight (mean \pm s.e.m., $n = 5$). FrC, fractional change (%).

cycling in cells. A split luciferase biosensor³⁰ was used to measure the interaction of KRAS with full length CRAF in live cells and to determine the effect of drug treatment over time (Fig. 4c). The drug disrupted the KRAS–CRAF complex with a rate constant of roughly 0.2 min^{-1} for WT KRAS and an average rate constant of $0.05 \pm 0.01 \text{ min}^{-1}$ for KRAS mutants (G12C/D/V, G13C/D and Q61H). In agreement, target inhibition was less potent in KRAS mutant models (Fig. 4a, mean IC_{50} of roughly 1 nM for WT and roughly 12 nM for mutant models and Extended Data Fig. 6b–d). Together, the data indicate that, rather than being fixed in an active state, common KRAS mutants undergo nucleotide cycling in cancer cells (a property that is necessary for the drug to access the GDP-bound conformation). The data also argue that KRAS mutants cycle with slower kinetics than WT KRAS.

KRASi treatment inhibited ERK and RSK phosphorylation predominantly in KRAS mutant models (mean IC_{50} roughly 150 nM for pERK and roughly 70 nM for pRSK), with only a small effect in WT or UAWT models (mean $IC_{50} > 10 \mu\text{M}$ for either intermediate, Fig. 4a and Extended

Data Fig. 5). KRASi treatment in the latter models led to an induction of N/HRAS-GTP amounts, an effect that was attenuated at higher drug concentrations (Extended Data Fig. 7a). Pan-KRASi treatment induced the formation of a complex between the catalytic subunit of SOS1 (SOScat) and H/NRAS, while displacing SOScat from KRAS (Extended Data Fig. 7b). Furthermore, the KRASi was able to inhibit ERK signalling and proliferation in KRAS WT cells with small-interfering RNA-mediated down-regulation of N/HRAS (Extended Data Fig. 7c,d). The data thus indicate that the lack of downstream signalling inhibition in KRAS WT models is probably due to compensation by HRAS and NRAS. They also argue for a tight balance and cross-regulation between RAS isoforms with the potential to confer a wide therapeutic index in patients.

To evaluate the effect on downstream signalling more broadly, and to identify transcripts and pathways immediately deregulated following KRAS inactivation, we carried out RNA sequencing (RNA-seq) in 22 models treated with either DMSO or KRASi for 2 h (Extended Data Fig. 8a). Most differentially expressed genes during KRASi treatment

were shared among KRAS mutant models, and only a small subset showed a pattern specific for a single mutant (Extended Data Fig. 8b). We next evaluated the effect of KRASi treatment on key RAS effector pathways by relying on experimentally derived transcriptional output signatures (Methods). As shown in Fig. 4d, KRASi treatment suppressed MEK/ERKi down-regulated genes, while inducing MEK/ERKi up-regulated genes. This effect was, again, more pronounced in cells with mutant as compared to WT KRAS (false discovery rate (FDR) <0.001 for down-regulated and FDR < 0.02 for up-regulated genes). KRASi treatment had a very small, if any, effect on PI3K, AKT and/or RAL signalling output in the models examined here (Fig. 4d). The mitogen-activated protein kinase (MAPK)-independent portion of the KRAS transcriptional output overlapped with signalling driven by extracellular ligands (Extended Data Fig. 8c).

The ability of the KRASi to suppress MAPK output more potently in KRAS mutant models correlated, on average, with a more potent antiproliferative effect in a panel of 274 cancer cell lines (Fig. 4e and Extended Data Fig. 9a–c). KRAS amplified cell lines also had on average a lower IC₅₀, as compared to models with WT KRAS (Fig. 4e, dedicated manuscript in preparation). The antiproliferative effect of treatment varied in KRAS mutant models, a finding that is in agreement with previous reports suggesting that only some KRAS mutant tumours depend on KRAS for their growth^{31,32}. Models harbouring a KRAS G12R or a KRAS Q61L/K/R mutation had little inhibition by the KRASi (Fig. 4a,b and Extended Data Fig. 9d). Furthermore, serum-deprivation enhanced the potency of inhibition (Extended Data Fig. 9e), an observation that is again consistent with the inactive state selective drug trapping mechanism (considering that serum withdrawal diminishes growth factor-driven nucleotide exchange). Drug treatment led to an increase in caspase activation in models harbouring a KRAS mutation but not in cells with WT KRAS (Extended Data Fig. 9f). In agreement with the data above, the inhibitory effect of the pan-KRASi on signalling and proliferation was attenuated in A59G double mutants (Extended Data Fig. 9g–i).

BI-2493 is a structural analogue of BI-2865 that was optimized for in vivo administration. The two pan-KRASi had a similar binding mode to mutant KRAS (Extended Data Fig. 10a,b) as well as similar inhibitory properties in RASless MEFs and cancer cell lines (Extended Data Fig. 10c–e). BI-2493 was highly selective for KRAS and did not cause more than 30% inhibition in a panel of 404 kinases or 38 targets commonly used in safety profiling (Extended Data Fig. 10f,g, respectively). Last, the inhibitor attenuated tumour growth in mice bearing KRAS G12C, G12D, G12V and A146V mutant models (Fig. 4f), without causing apparent toxicity to the mice (at least as determined by monitoring animal weight). The antitumor effects were associated with favourable pharmacokinetic properties, as evidenced by the amount of drug exposure in both plasma and tumour (Extended Data Fig. 10h,i), as well as a concordant inhibition of ERK phosphorylation and *DUSP6* messenger RNA expression in tumour models (Extended Data Fig. 10j).

Here we report the discovery of a pan-KRAS inhibitor that inactivates common KRAS oncproteins without needing to be covalently anchored to a specific mutant amino acid (Supplementary Discussion). Selectivity for KRAS was conferred through direct and/or indirect constraints imposed by three G domain residues that show evolutionary divergence between RAS isoforms. The pan-KRAS inhibitor works by preferentially targeting the inactive state of KRAS to prevent its reactivation by nucleotide exchange. In cells with mutant KRAS, this led to suppressed downstream signalling and cancer cell growth, suggesting that common KRAS mutants found in cancer depend on nucleotide exchange for activation. In cells with WT KRAS, drug treatment led to an increase in the activation of other RAS isoforms, which limit the antiproliferative effect of treatment (Extended Data Fig. 7a). The cellular effects of the pan-KRAS inhibitor argue that susceptibility to inactive state selective inhibition is not a unique property of KRAS G12C but one that can be applied to broadly target KRAS mutants. The latter include G12A/C/D/F/V/S, G13C/D, V14I, L19F, Q22K, D33E, Q61H, K117N and

A146V/T, which together comprise most of the KRAS mutants found in cancer.

Our study serves as a blueprint for the development of more KRAS directed therapeutics, including small molecule inhibitors of GTP-bound KRAS and proteolysis targeting chimeras. Pan-KRAS inhibitors, such as the one described here, merit clinical testing in patients as they stand to affect the clinical outcomes of patients with KRAS-driven cancers, including those with lung, colorectal and pancreatic cancer as well as further less-frequent cancer types. Selective inhibition of KRAS, while sparing HRAS and NRAS, a property that differentiates our inhibitor from other emerging drugs, is likely to produce a wide therapeutic index in the clinic.

Online content

Any methods, additional references, Nature Portfolio reporting summaries, source data, extended data, supplementary information, acknowledgements, peer review information; details of author contributions and competing interests; and statements of data and code availability are available at <https://doi.org/10.1038/s41586-023-06123-3>.

- Ostrem, J. M., Peters, U., Sos, M. L., Wells, J. A. & Shokat, K. M. K-Ras(G12C) inhibitors allosterically control GTP affinity and effector interactions. *Nature* **503**, 548–551 (2013).
- Lito, P., Solomon, M., Li, L. S., Hansen, R. & Rosen, N. Allele-specific inhibitors inactivate mutant KRAS G12C by a trapping mechanism. *Science* **351**, 604–608 (2016).
- Canon, J. et al. The clinical KRAS(G12C) inhibitor AMG 510 drives anti-tumour immunity. *Nature* **575**, 217–223 (2019).
- Hallin, J. et al. The KRAS(G12C) inhibitor MRTX849 provides insight toward therapeutic susceptibility of KRAS-mutant cancers in mouse models and patients. *Cancer Discov.* **10**, 54–71 (2020).
- Hong, D. S. et al. KRAS(G12C) inhibition with sotorasib in advanced solid tumors. *N. Engl. J. Med.* **383**, 1207–1217 (2020).
- Skoulidis, F. et al. Sotorasib for lung cancers with KRAS p.G12C mutation. *N. Engl. J. Med.* **384**, 2371–2381 (2021).
- Janne, P. A. et al. Adagrasib in non-small-cell lung cancer harboring a KRAS(G12C) mutation. *N. Engl. J. Med.* **387**, 120–131 (2022).
- Malumbres, M. & Barbacid, M. RAS oncogenes: the first 30 years. *Nat. Rev. Cancer* **3**, 459–465 (2003).
- Pylayeva-Gupta, Y., Grabocka, E. & Bar-Sagi, D. RAS oncogenes: weaving a tumorigenic web. *Nat. Rev. Cancer* **11**, 761–774 (2011).
- Simanshu, D. K., Nissley, D. V. & McCormick, F. RAS proteins and their regulators in human disease. *Cell* **170**, 17–33 (2017).
- Hofmann, M. H., Gerlach, D., Misale, S., Petronczki, M. & Kraut, N. Expanding the reach of precision oncology by drugging all KRAS mutants. *Cancer Discov.* **12**, 924–937 (2022).
- Punekar, S. R., Velcheti, V., Neel, B. G. & Wong, K. K. The current state of the art and future trends in RAS-targeted cancer therapies. *Nat. Rev. Clin. Oncol.* <https://doi.org/10.1038/s41571-022-00671-9> (2022).
- Trahey, M. & McCormick, F. A cytoplasmic protein stimulates normal N-ras p21 GTPase, but does not affect oncogenic mutants. *Science* **238**, 542–545 (1987).
- Margarit, S. M. et al. Structural evidence for feedback activation by Ras.GTP of the Ras-specific nucleotide exchange factor SOS. *Cell* **112**, 685–695 (2003).
- Li, C. et al. The G protein signaling regulator RGS3 enhances the GTPase activity of KRAS. *Science* **374**, 197–201 (2021).
- Bollag, G. et al. Biochemical characterization of a novel KRAS insertion mutation from a human leukemia. *J. Biol. Chem.* **271**, 32491–32494 (1996).
- Ahmadian, M. R. et al. Guanosine triphosphatase stimulation of oncogenic Ras mutants. *Proc. Natl. Acad. Sci. USA* **96**, 7065–7070 (1999).
- Wey, M., Lee, J., Jeong, S. S., Kim, J. & Heo, J. Kinetic mechanisms of mutation-dependent Harvey Ras activation and their relevance for the development of Costello syndrome. *Biochemistry* **52**, 8465–8479 (2013).
- Hunter, J. C. et al. Biochemical and structural analysis of common cancer-associated KRAS mutations. *Mol. Cancer Res.* **13**, 1325–1335 (2015).
- Kano, Y. et al. Tyrosyl phosphorylation of KRAS stalls GTPase cycle via alteration of switch I and II conformation. *Nat. Commun.* **10**, 224 (2019).
- Killoran, R. C. & Smith, M. J. Conformational resolution of nucleotide cycling and effector interactions for multiple small GTPases determined in parallel. *J. Biol. Chem.* **294**, 9937–9948 (2019).
- Patricelli, M. P. et al. Selective inhibition of oncogenic KRAS output with small molecules targeting the inactive state. *Cancer Discov.* **6**, 316–329 (2016).
- Janes, M. R. et al. Targeting KRAS mutant cancers with a covalent G12C-specific inhibitor. *Cell* **172**, 578–589 e517 (2018).
- Hall, B. E., Bar-Sagi, D. & Nassar, N. The structural basis for the transition from Ras-GTP to Ras-GDP. *Proc. Natl. Acad. Sci. USA* **99**, 12138–12142 (2002).
- Drosten, M. et al. Genetic analysis of Ras signalling pathways in cell proliferation, migration and survival. *EMBO J.* **29**, 1091–1104 (2010).
- Awad, M. M. et al. Acquired resistance to KRAS(G12C) inhibition in cancer. *N. Engl. J. Med.* **384**, 2382–2393 (2021).

Article

27. Feng, S. et al. A saturation mutagenesis screen uncovers resistant and sensitizing secondary KRAS mutations to clinical KRAS(G12C) inhibitors. *Proc. Natl Acad. Sci. USA* **119**, e2120512119 (2022).
28. Tanaka, N. et al. Clinical acquired resistance to KRAS(G12C) inhibition through a novel KRAS switch-II pocket mutation and polyclonal alterations converging on RAS-MAPK reactivation. *Cancer Discov.* **11**, 1913–1922 (2021).
29. Osaka, N. et al. Divergent mechanisms activating RAS and small GTPases through post-translational modification. *Front. Mol. Biosci.* **8**, 707439 (2021).
30. Cooley, R. et al. Development of a cell-free split-luciferase biochemical assay as a tool for screening for inhibitors of challenging protein-protein interaction targets. *Wellcome Open Res.* **5**, 20 (2020).
31. Singh, A. et al. TAK1 inhibition promotes apoptosis in KRAS-dependent colon cancers. *Cell* **148**, 639–650 (2012).
32. Singh, A. et al. A gene expression signature associated with “K-Ras addiction” reveals regulators of EMT and tumor cell survival. *Cancer Cell* **39**, 441–442 (2021).

Publisher's note Springer Nature remains neutral with regard to jurisdictional claims in published maps and institutional affiliations.



Open Access This article is licensed under a Creative Commons Attribution 4.0 International License, which permits use, sharing, adaptation, distribution and reproduction in any medium or format, as long as you give appropriate credit to the original author(s) and the source, provide a link to the Creative Commons licence, and indicate if changes were made. The images or other third party material in this article are included in the article's Creative Commons licence, unless indicated otherwise in a credit line to the material. If material is not included in the article's Creative Commons licence and your intended use is not permitted by statutory regulation or exceeds the permitted use, you will need to obtain permission directly from the copyright holder. To view a copy of this licence, visit <http://creativecommons.org/licenses/by/4.0/>.

© The Author(s) 2023

Methods

Cell culture and reagents

The cell lines used in the study were maintained in DMEM medium supplemented with 10% FBS, penicillin, streptomycin and 2 mM L-glutamine. Cells were obtained from ATCC and tested negative for mycoplasma. Sotorasib was purchased from Selleckchem.

Immunoblotting

Cells were gathered and lysed with NP40 lysis buffer (50 mM Tris pH 7.5, 1% NP40, 150 mM NaCl, 10% glycerol and 1 mM EDTA) containing protease (Pierce Protease Inhibitor Mini Tablets, Thermo Fisher Scientific no. 88665) and phosphatase (Pierce Phosphatase Inhibitor Mini Tablets, Thermo Fisher Scientific no. 88667) inhibitors on ice for 10 min. After that, the lysates were centrifuged at 16,000g for 10 min before protein concentration was quantified by the BCA assay (Thermo Fisher Scientific). The proteins were resolved on 4–12% SDS-PAGE gels (Thermo Fisher Scientific) in 1× MOPS buffer (Thermo Fisher Scientific) at 90–120 constant voltage (V) and transferred to nitrocellulose membranes (GE Healthcare) with 1× Tris-Glycine Buffer (BioRad) at 100 V for 1 h. Membranes were blocked in 5% non-fat milk for 1 h and then probed with primary antibodies overnight at 4 °C and visualized using horseradish peroxidase (HRP)-conjugated secondary antibodies and extracellular ligands (Thermo Fisher Scientific). Primary antibodies used to detect NRAS (sc-519) or HRAS (18295-1-AP) were obtained from Santa Cruz Biotechnology or Proteintech, respectively. Those used for the detection of phospho-ERK (9101), ERK (4696), phospho-RSK(Thr359) (8753), RSK (9355), β-actin (4970) and HA (3724) were obtained from Cell Signaling Technology. Antibodies used to detect KRAS (WH0003845M1) were obtained from Millipore Sigma and the antibody detecting CRAF (610152) was purchased from BD Bioscience. Immunoblots were quantified using ImageJ.

RAS activation assay

RAS activity was detected using the active Ras pull-down and detection kit (Thermo Fisher Scientific). Briefly, GST-RAF1RBD and glutathione agarose resin were mixed with whole-cell lysates and incubated on a rotator for 1 h at 4 °C, followed by three washes and elution with 2× SDS-PAGE loading buffer. The samples were then analysed by SDS-PAGE and western blotting with a KRAS-specific antibody (2F2, Sigma). When epitope-tagged KRAS, NRAS and/or HRAS variants were exogenously expressed, an epitope-specific antibody enabled specific determination of these variants in their GTP-bound conformation.

Protein expression and purification

Each RAS gene (K, N or HRAS) was cloned into pET28a vector with an N-terminal His6 tag. SOScat (566–1049 amino acids (aa)) was cloned into pGEX-4T-1 vector with a N-terminal GST tag. Each gene was expressed in *Escherichia coli* BL21 cells, cultured in Terrific Broth media overnight and induced with 0.5 mM isopropyl-β-D-thiogalactosid at 18 °C. The cells were lysed in binding buffer (50 mM Tris-HCl pH 7.5, 0.25 M NaCl, 10% glycerol, 10 mM imidazole, 1 mM benzamidine, 1 mM phenylmethylsulfonyl fluoride, 5 mM β-mercaptoethanol) and the extracts were subjected to affinity purification by using nickel-nitrilotriacetic acid (Gold Bio) or a glutathione column (GE healthcare). His-tagged proteins were eluted in 250 mM imidazole and GST-tagged proteins were eluted in 25 mM reduced glutathione (pH 8.8). Eluted fractions were subjected to a second round of purification by size-exclusion chromatography by using a Sephadryl 200 size-exclusion column (Cytiva) in a buffer containing 25 mM Tris-HCl, pH 7.5, 150 mM NaCl, 1 mM dithiothreitol and 5% glycerol.

Nucleotide exchange

Nucleotide exchange was measured through exchange of GDP to GTP-DY-647P1 by using a Homogeneous Time Resolved Fluorescence

assay (Ex/Em: 337/665; 620) in PHERAstar (BMG Labtech). GST-tagged RAS was mixed with α-GST-Tb antibody (1.5× solution) and a 10 µl sample was delivered to reaction wells. The inhibitors were tested in ten different concentrations with threefold serial dilution from 10 µM, and were delivered to reaction wells using an acoustic dispenser (Echo, Labcyte). The RAS/GST-Tb antibody and inhibitor mixture was pre-incubated for 1 h at room temperature before reaction. Then, 5 µl of GTP-DY-647P1 (final 0.15 µM) and SOScat (564–1049 aa) were added to reaction well to initiate the exchange reaction. In each reaction, 10–30 nM of RAS and 5–150 nM of SOScat were used.

ITC

Calorimetric experiments of the pan-KRASi (BI-2865) were performed on a MicroCal PEAQ-ITC instrument (Malvern Panalytical Ltd). Protein solutions were buffer exchanged by dialysis into buffer containing 20 mM HEPES pH 7.6, 130 mM sodium chloride, 2 mM magnesium chloride and 0.5 mM TCEP. All measurements were carried out at 23 °C. Titrand and titrator concentrations were adjusted to 3% DMSO. The cell was loaded with protein solutions in the range of 0 to 40 µM. All injections were performed using an initial injection of 0.5 µl followed by 19 injections of 2 µl of compound in the range of 100–500 µM. The data were analysed with the MicroCal PEAQ-ITC analysis software package (v.1.1.0.1262). The first data point was excluded from the analysis. Thermodynamic parameters were calculated by the following formula: $\Delta G = \Delta H - T\Delta S = -RT\ln K_d$, where ΔG , ΔH and ΔS are the changes in free energy, enthalpy and entropy of binding, respectively, T is the temperature, and R is the universal gas constant (Supplementary Fig. 2).

Surface plasmon resonance

Surface plasmon resonance experiments were performed on Biacore 8K instruments (Cytiva). Streptavidin (Prospec) was immobilized at 25 °C on CM5 Chips (Cytiva) using 10 mM HBS-P+ buffer (pH 7.4) (Cytiva). The surface was activated using 400 mM 1-ethyl-3-(3-dimethylaminopropyl)-carbodiimide and 100 mM N-hydroxysuccinimide (Cytiva) (contact time 420 s, flow rate 10 ml min⁻¹). Streptavidin was diluted to a final concentration of 1 mg ml⁻¹ in 10 mM sodium acetate (pH 5.0) and injected for 600 s. The surface was subsequently deactivated by injecting 1 M ethanolamine for 420 s and conditioned by injecting 50 mM NaOH and 1 M NaCl. Dilution of the biotinylated target proteins and streptavidin coupling was performed using running buffer without DMSO. The target proteins were prepared at 0.1 mg ml⁻¹ and coupled to a density between 200 and 800 response units. All interaction experiments were performed at 25 °C in running buffer (20 mM Tris(hydroxymethyl)aminomethane, 150 mM potassium chloride, 2 mM magnesium chloride, 2 mM Tris(2-carboxyethyl)phosphine hydrochloride, 0.005% Tween20, 40 µM Guanosine 5'-diphosphate, pH 8.0, 1% DMSO). The compounds were diluted in running buffer and injected over the immobilized target proteins (concentration range for KRAS mutants, 6.25–1,000 nM). Sensorsgrams from reference surfaces and blank injections were subtracted from the raw data before data analysis using Biacore Insight software. Affinity and binding kinetic parameters were determined by using a 1/1 interaction model, with a term for mass transport included (Supplementary Fig. 3).

Protein preparation and crystallization

KRAS WT, G12C, G12D, G12V, G13D and respective biotinylated versions (for each, amino acids 1–169 of UniProt sequence P01116) were cloned, expressed and purified as previously described³³. Crystals of BI-2865 in complex with the variants above were obtained by cocrystallization. Protein solutions of KRAS WT (42 mg ml⁻¹), G12C (38 mg ml⁻¹), G12D (40 mg ml⁻¹), G12V (48 mg ml⁻¹), G13D (41 mg ml⁻¹) in 20 mM Tris; 150 mM NaCl; 2 mM TCEP; 2 mM MgCl₂; pH 7.5 were incubated with 2 mM BI-2865 and 4% DMSO. Crystals were obtained using the hanging drop method, by mixing 1 µl of protein solution with 1 µl of reservoir

Article

solution (0.2 mM MgCl₂, 15–27% PEG 2000, 100 mM sodium acetate pH 4.4) at 4 °C. Plate-like crystals appeared overnight and were flash frozen in liquid nitrogen using 25–30% ethylene glycol in the reservoir as a cryoprotectant. Crystals belonged to same space group P2₁2₁2₁ containing one monomer in the asymmetric unit. Diffraction data was collected at X06SA beamline of the Swiss Light Source (Paul Scherrer Institute). Images were processed with autoPROC³⁴ and all structures were solved by molecular replacement using a previously solved structure. Model building and refinement was performed with standard protocols using CCP4, COOT, autoBUSTER v.2.11.2 (<http://www.globalphasing.com>) and Phenix^{35,36}. Data collection and refinement statistics are shown in Extended Data Table 1. The Fo–Fc electron density maps, obtained by a simulated annealing protocol, of the respective structures are shown in Supplementary Fig. 1.

Cell viability assay and cell proliferation assays

Individual cancer cell lines. The cells were seeded in 96-well plates at 2,000 cells per well in triplicates (at the minimum) and treated with the indicated concentrations of BI-2865. After 72 h, cell viability was assayed by CellTiter-Glo Luminescent Cell Viability Assay (Promega). The background value (media without cells) was subtracted from the raw data and fold change was calculated relative to time zero.

Isogenic BaF3 cells. In brief, BaF3 cells were transduced with a virus derived from plasmids expressing KRAS G12C, G12D or G12V mutants (pMSCV-KRAS-PGK-Puro-IRES-GFP). The transduction efficacy was monitored by fluorescence-activated cell sorting. Cells were selected in puromycin (1 µg ml⁻¹) and IL-3 (10 ng ml⁻¹) for 1–2 weeks or until control cells were dead. This was followed by withdrawal of IL-3 and several passages in the absence of IL-3. Integration of the exogenous KRAS was confirmed by sequencing. To determine the effect of drug treatment on proliferation, 1,500 cells were plated in 384-well plates in 60 µl of Roswell Park Memorial Institute medium (10% FCS) and kept overnight at 37 °C. Cell viability was determined as above.

High-throughput screen of the 274 cell line panel. This was performed at Horizon Discovery. Briefly, the cells were seeded in 25 µl of growth media in black 384-well tissue culture plates at the density defined for the respective cell line and plates were placed at 37 °C, 5% CO₂ for 24 h before treatment. At the time of treatment, a set of assay plates (which did not receive treatment) were collected and ATP concentrations were measured by using CellTiter-Glo v.2.0 (Promega) and luminescence reading on an Envision plate reader (Perkin Elmer). BI-2493 (a structurally similar analogue of BI-2865), was transferred to assay plates using an Echo acoustic liquid handling system. Assay plates were incubated with the compound for 5 days and were then analysed by using CellTiter-Glo. All data points were collected by means of automated processes and were subject to quality control and analysed using Horizon's proprietary software. Horizon uses growth inhibition as a measure of cell growth. The growth inhibition percentages were calculated by applying the following test and equation: if $T < V_0$ then $100(1 - (T - V_0)/V_0)$ and if $T \geq V_0$ then $100(1 - (T - V_0)/(V - V_0))$, where T is the signal measure for a test article, V is the untreated or vehicle-treated control measure and V_0 is the untreated or vehicle-treated control measure at time zero (colloquially referred to as T0 plates). This formula was derived from the Growth Inhibition (GI) calculation used in the National Cancer Institute's NCI-60 high-throughput screen.

Saturation mutagenesis

To generate the saturation mutagenesis library, the DNA sequence of KRAS G12C (codon 2–188) was mutated to encode for all possible amino acids. The DNA sequence was codon-optimized for expression in human cells. The library DNA was then subcloned into the pLIX_403 lentiviral expression vector (Addgene, no. 41395). Lentivirus was produced by

transfecting the library DNA along with packaging (psPAX2) and envelope (pMD2.G) plasmid into HEK293T cells. The virus was collected at 48 h after transfection, aliquoted and snap-frozen in liquid nitrogen and stored at –80 °C. The saturation mutagenesis screen was performed in the NCI-H358 cell line (ATCC, CRL-5807). The cells were transduced with the lentivirus library at a multiplicity of infection of 0.5 with polybrene (Millipore) at 0.8 µg ml⁻¹. After selection with puromycin (2 µg ml⁻¹), live cells were collected and separated into three equal fractions (4 million cells per fraction). One fraction was pelleted and frozen at –80 °C (day 0). Another fraction was propagated in cell culture in the presence of doxycycline (1 µg ml⁻¹) and DMSO. The third fraction was propagated in the presence of dox and the pan-KRASi (BI-2865, 10 µM). The cells were passaged when reaching confluence. The media was refreshed every 3 days. The cells were collected and pelleted after 14 days of treatment. The screen was performed in biological triplicates. Genomic DNA from pelleted cells was extracted with the DNeasy blood and tissue kit (Qiagen) and used as template to amplify the mutagenesis library. The following primers were used: forward 5'-tttagtgaaccgtcagatcgctgg-3' and reverse 5'-gaaagctgaacccggatccccgtca-3'. The PCR products were purified using agarose gel electrophoresis and the QIAquick Gel Extraction kit (Qiagen). Purified PCR products were subjected to Nextera reactions according to the Illumina Nextera XT protocol. The samples were indexed and purified with the Agencourt AMPure XP kit before being subjected to HiSeq analysis at 2 × 150 bp. Count files were generated by using the ORFcall software (Broad Institute) and aligned to the KRAS G12C reference sequence. The raw read counts of each treatment groups were analysed using edgeR to determine the log₂ fold change between the reads at day 14 relative to day 0.

RNA-seq

HEK293 (WT), MRC5 (WT), MRC9 (WT), PC9 (UAWT), HCC827 (UAWT), H1650 (UAWT), H358 (G12C), H2122 (G12C), CALU1 (G12C), MIAPAC2 (G12C), LS513 (G12D), HPAC (G12D), ASPC1 (G12D), PANC1 (G12D), PANC0403 (G12D), H727 (G12V), CAPAN1 (G12V), SW620 (G12V), SW480 (G12V), LOVO (G13D), DLD1 (G13D) and HCT116 (G13D) cells were treated with the KRAS inhibitor (BI-2865, 5 µM) or DMSO for 2 h in biological duplicates for each condition. RNA was extracted using RNeasy Mini Kit (Qiagen catalogue no. 74104) according to the manufacturer's instructions. After RiboGreen quantification and quality control by Agilent BioAnalyzer, 500 ng of total RNA per sample underwent polyA selection and TruSeq library preparation according to instructions provided by Illumina (TruSeq Stranded mRNA LT Kit, catalogue no. RS-122-2102), with eight cycles of PCR. Samples were barcoded and run on HiSeq 4000 in a 50/50 bp paired end run, with an average of 30 million paired reads per sample. Ribosomal reads represented less than 0.5% of the total reads generated. The sequencing output files from different lanes were concatenated, aligned to GRCh38 using HISAT2 and transcripts were counted using HTSeq in Python. The count data matrix was then processed by using limma and edgeR in R/Bioconductor, as described. Briefly, the data were filtered by removing transcripts that were not detected in all replicates. Size factor normalization was carried out and differential expression analysis was carried out contrasting each time point to the untreated condition. The count data were transformed to log₂ counts per million followed by an estimation of the mean-variance relationship. The data for each gene was used to fit a linear model and to compute various statistical parameters for a given set of contrasts. Correction for multiple hypothesis testing was carried out using the FDR method. Differential expression genes were considered those with absolute scaled log₂ fold change of equal or greater than 2.56 (or more than three standard deviations from the mean) and an adjusted P value of less than 0.05. The heat map in Extended Data Fig. 8a shows the top 50 differential expression genes following KRASi treatment while blocking for cell line of origin (that is, shared output). The annotation rows show the trend (up- or down-regulation) in the effect of KRASi over DMSO or in the effect of KRASi in mutant trait over WT models.

Effector output score. The output score for the main RAS effector pathways, that is, RAF/MEK/ERK, PI3K/AKT and RAL, H358 (KRAS G12C) mutant cells were treated with DMSO or inhibitors targeting MEK (trametinib, 25 nM), ERK (SCH984, 500 nM), PI3K (BYL719, 1 μM), AKT (MK2206, 1 μM) or RAL (BQ757, 10 μM) for 4 h. RNA extracted from cells subjected to these treatments was sequenced and analysed as described above. Differential expression genes in drug versus DMSO comparisons were those with an absolute scaled logFC of greater than 2.56 and a FDR < 0.05. These genes were then used to determine the effect of KRASi treatment on RAS effector signalling pathways. The output score determined by the average scaled logFC in the KRASi versus DMSO comparison for MEK, ERK, PI3K, AKT or RAL dependent genes. The up- and down-regulated effector output scores were calculated from genes that were, respectively, down- or up-regulated by inhibitors targeting the intermediates and the numbers of genes used to calculate the average score are shown in Fig. 4d. Statistical significance in effector output score in the KRASi versus DMSO comparison were established either by FGSEA or edgeR/camera in R. Statistical significance in the effect of KRASi in mutant trait versus WT models was established using edgeR/roast, also in R.

Mouse studies

These were carried out as described^{37–40}. Mice were housed according to the internal institutional and Austrian governmental and European Union guidelines (Austrian Animal Protection Laws, ETS-123) at Boehringer Ingelheim or according to the Institutional Animal Care and Use Committee guidelines at MSKCC. All animal studies were approved by the internal ethics and the local governmental committee. To establish cell line-derived xenograft models, 7–8-week-old female NMRI nude (BomTac:NMRI-Foxn1nu) mice with a bodyweight of 20 g from Taconic were engrafted subcutaneously with 5 million (LS513, GP2d, HPAC, SW620) or 10 million cells (MIAPACA2), respectively, suspended in growth factor reduced, phenol red-free Matrigel (Corning) (LS513, GP2d, HPAC, SW620) or in PBS/5% FBS (SW620). Mice were group-housed under pathogen-free and controlled environmental conditions ($21 \pm 1.5^\circ\text{C}$ temperature, $55 \pm 10\%$ humidity and a 12 h light–dark cycle). Once tumours reached roughly 200 mm^3 volume, mice were randomized on the basis of tumour size ($n = 7$ –8 mice per treatment arm) and treated with drug or vehicle control (0.5% Natrosol/5% HPβCD). The inhibitor used for in vivo studies was a structurally similar analogue of BI-2865 dosed at 90 mg per kg twice daily (BI-2493). Treatment was administered by oral gavage using an application volume of 10 ml per kg and the average tumour diameter (two perpendicular axes of the tumour were measured) was measured in control and treated groups using a calliper in a non-blinded manner by a research technician, who was not aware of the objectives of the study. Data analysis was done by Prism (GraphPad Software). The pan-KRAS inhibitors described here (GDP-KRAS inhibitors) are available as part of a collaborative programme through Boehringer Ingelheim's open innovation portal opnMe.com: <https://opnme.com/collaborate-now/GDP-KRAS-inhibitor-bi-2493>.

Reporting summary

Further information on research design is available in the Nature Portfolio Reporting Summary linked to this article.

Data availability

Atomic coordinates and structure factors for the cocrystal structures have been deposited in the Protein Data Bank with accession codes 8AZR, 8AZV, 8AZX, 8AZY, 8AZZ and 8B00. Raw data from sequencing analyses can be found in the supplementary material. Raw files have been deposited in the National Center for Biotechnology Information Gene Expression Omnibus (GSE228010). Source data are provided with this paper.

Code availability

The data were analysed by using publicly available code.

33. Kessler, D. et al. Drugging an undruggable pocket on KRAS. *Proc. Natl. Acad. Sci. USA* **116**, 15823–15829 (2019).
34. Vonrhein, C. et al. Data processing and analysis with the autoPROC toolbox. *Acta Crystallogr. D. Biol. Crystallogr.* **67**, 293–302 (2011).
35. Collaborative Computational Project, N. The CCP4 suite: programs for protein crystallography. *Acta Crystallogr. D. Biol. Crystallogr.* **50**, 760–763 (1994).
36. Emsley, P., Lohkamp, B., Scott, W. G. & Cowtan, K. Features and development of Coot. *Acta Crystallogr. D. Biol. Crystallogr.* **66**, 486–501 (2010).
37. Xue, Y. et al. An approach to suppress the evolution of resistance in BRAF(V600E)-mutant cancer. *Nat. Med.* **23**, 929–937 (2017).
38. Xue, J. Y. et al. Rapid non-uniform adaptation to conformation-specific KRAS(G12C) inhibition. *Nature* **577**, 421–425 (2020).
39. Hofmann, M. H. et al. BI-3406, a potent and selective SOS1-KRAS interaction inhibitor, is effective in KRAS-driven cancers through combined MEK inhibition. *Cancer Discov.* **11**, 142–157 (2021).
40. Zhao, Y. et al. Diverse alterations associated with resistance to KRAS(G12C) inhibition. *Nature* **599**, 679–683 (2021).

Acknowledgements We thank F. Savarese for critical reading of the manuscript and for constructive input and M. Mroczkowski for her insight on the manuscript. We also thank J. Chodera for allowing the use of the ITC instrument. P.L. is supported in part by the NIH/NCI (grant nos. 1R01CA23074501, 1R01CA23026701A1 and 1R01CA279264-01), The Pew Charitable Trusts, the Damon Runyon Cancer Research Foundation and the Pershing Square Sohn Cancer Research Alliance. We acknowledge the Josie Robertson Investigator Program and the Support Grant-Core Grant program (grant no. P30 CA008748) at the Memorial Sloan Kettering Cancer Center.

Author contributions D.K., L.H., D.R., N.K. and P.L. designed the study and analysed data. D.K., D.R., C.I.A.-S., A.V., B.S., A.C.-N., J.Y.X., C.L. and D.B.M. performed cell-based experiments and/or provided key scientific input. D.K. and D.R. helped perform in vivo studies. Y.P. assisted with protein purification and biochemical assays. L.H. and A.M. led the chemical synthesis efforts. Y.Z. and C.I.A.-S. carried out saturation mutagenesis studies and validation experiments. J.B. and B.W. carried out crystallization studies. J.B., B.W. and D.K. carried out ITC studies. J.P. and O.S. carried out pharmacokinetic or pharmacodynamic studies. K.G.K. carried out surface plasmon resonance studies. D.K., L.H., D.R., J.B., N.K. and P.L. were the main writers of the manuscript. All authors reviewed the manuscript and contributed to writing it.

Competing interests P.L. is listed as an inventor on patents filed by MSKCC on the treatment of KRAS or BRAF mutant cancers (US20200009138A1). P.L. reports grants to his institution from Amgen, Mirati, Revolution Medicines, Boehringer Ingelheim and Virtec Pharmaceuticals. P.L. reports consulting fees from Black Diamond Therapeutics, AmMax, OrbiMed, PAQTx, Repare Therapeutics and Revolution Medicines, travel reimbursement from Boehringer Ingelheim as well as membership of the Scientific Advisory Board of Frontier Medicines (consulting fees and equity). L.H., D.R., J.B., B.W., K.G.K., D.B.M. and N.K. are employed by Boehringer Ingelheim. The remaining authors declare no competing interests.

Additional information

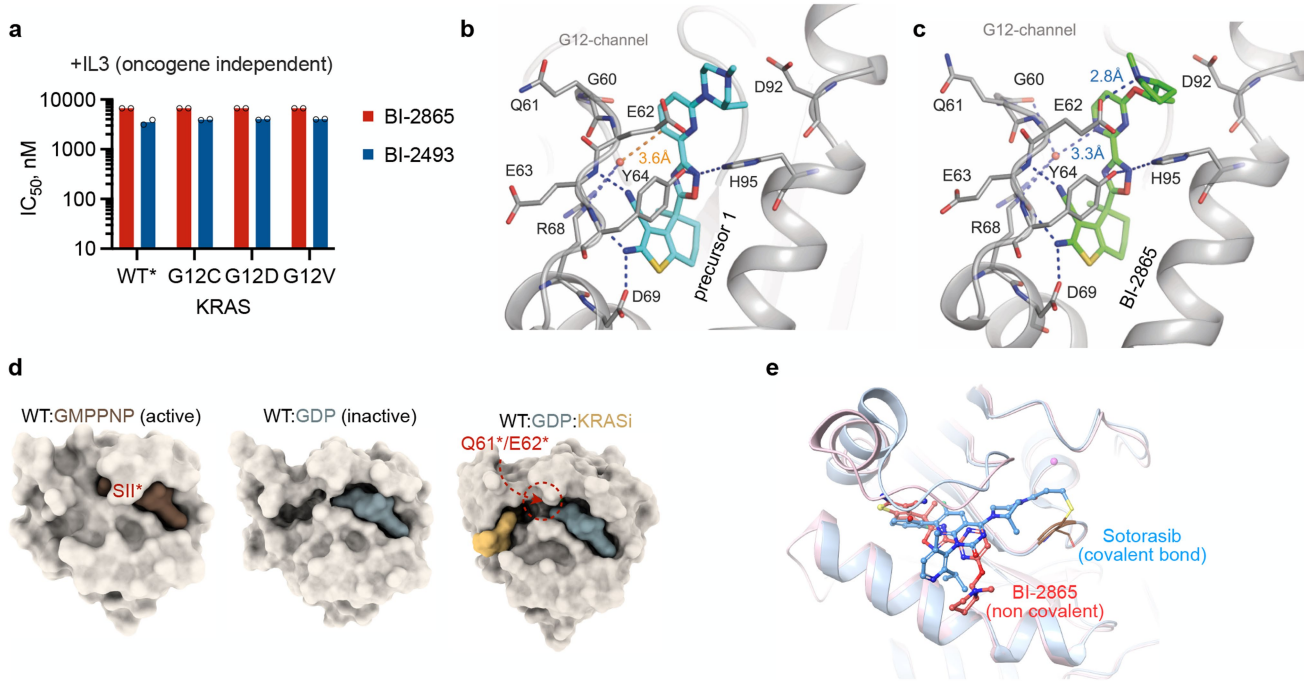
Supplementary information The online version contains supplementary material available at <https://doi.org/10.1038/s41586-023-06123-3>.

Correspondence and requests for materials should be addressed to Piro Lito.

Peer review information *Nature* thanks Jonathan Ostrem, Arvin C. Dar and the other, anonymous, reviewer(s) for their contribution to the peer review of this work.

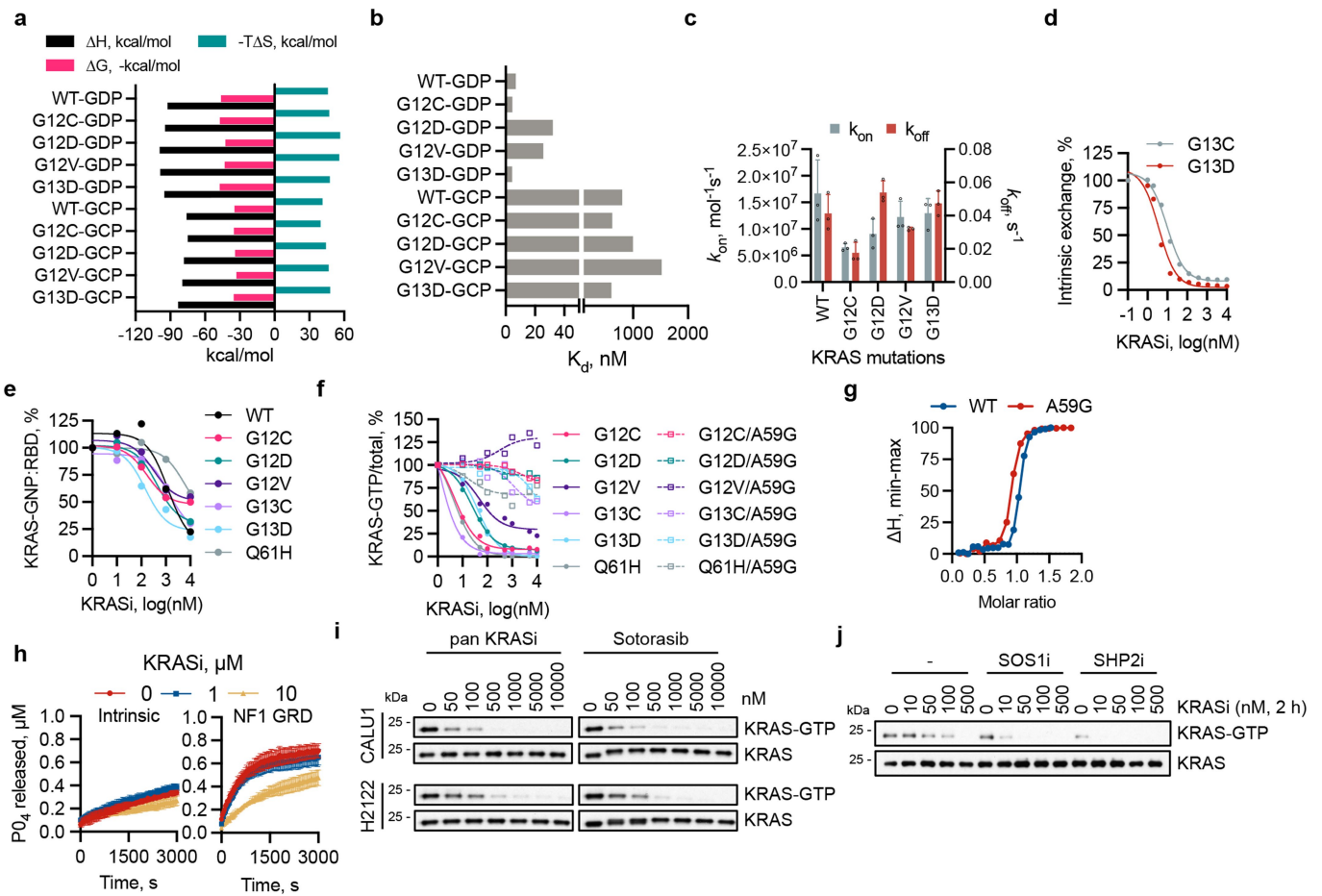
Reprints and permissions information is available at <http://www.nature.com/reprints>.

Article



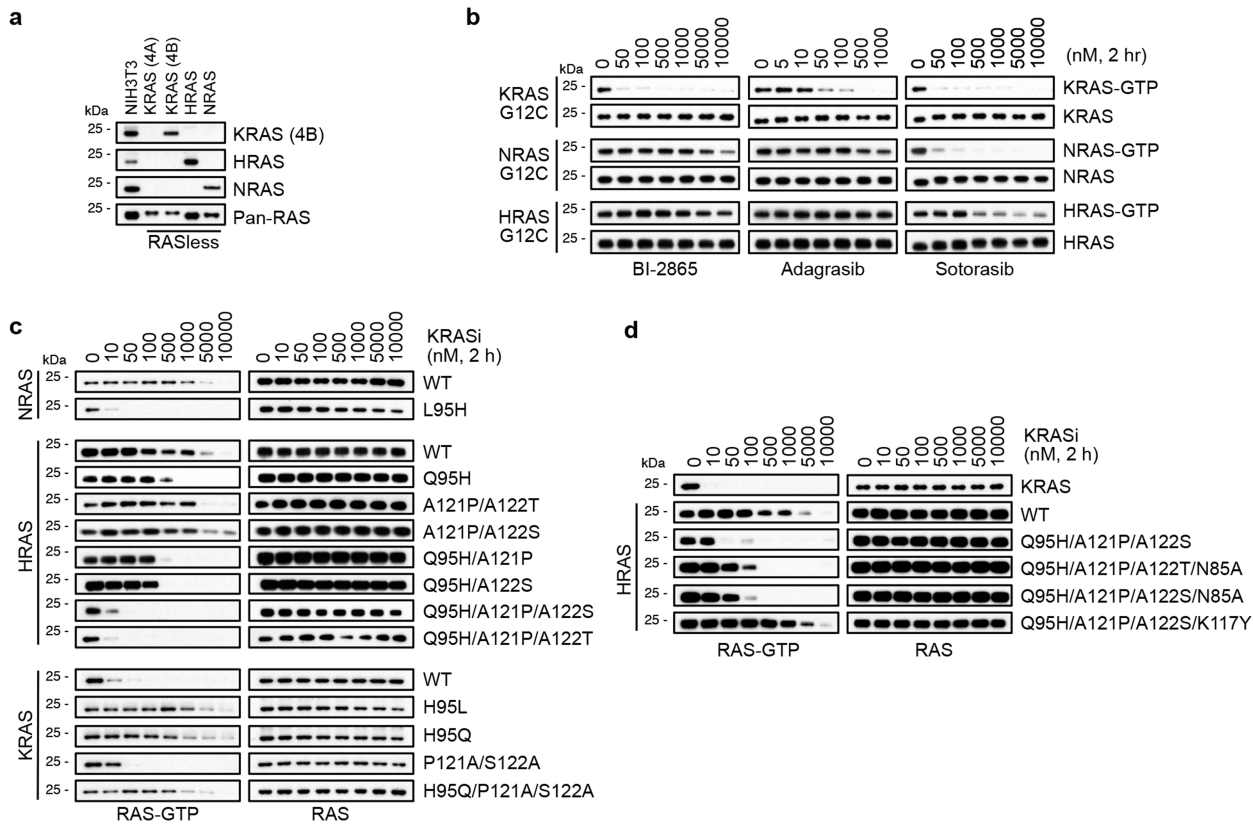
Extended Data Fig. 1 | Rational design of a non-covalent pan KRAS inhibitor. **a**, Isogenic BaF3 cells engineered to express the indicated KRAS variants were treated as shown for 72 h to determine the IC₅₀ ($n = 2$, mean and each replicate). IL3 stimulation was used to induce oncogene independent growth. The effect of treatment in the absence of IL3 is shown in Fig. 1b. *: endogenous KRAS WT.

b,c, Co-crystal structures of precursor 1 (b) or BI-2865 (c) bound to KRAS. **d**, Space filling models of KRAS variants in an apo- or drug-bound conformation. S:switch;*:active state conformation. **e**, Superimposition of co-crystal structures of KRAS G12C in complex with the covalent inhibitor sotorasib or the pan KRAS inhibitor BI-2865.



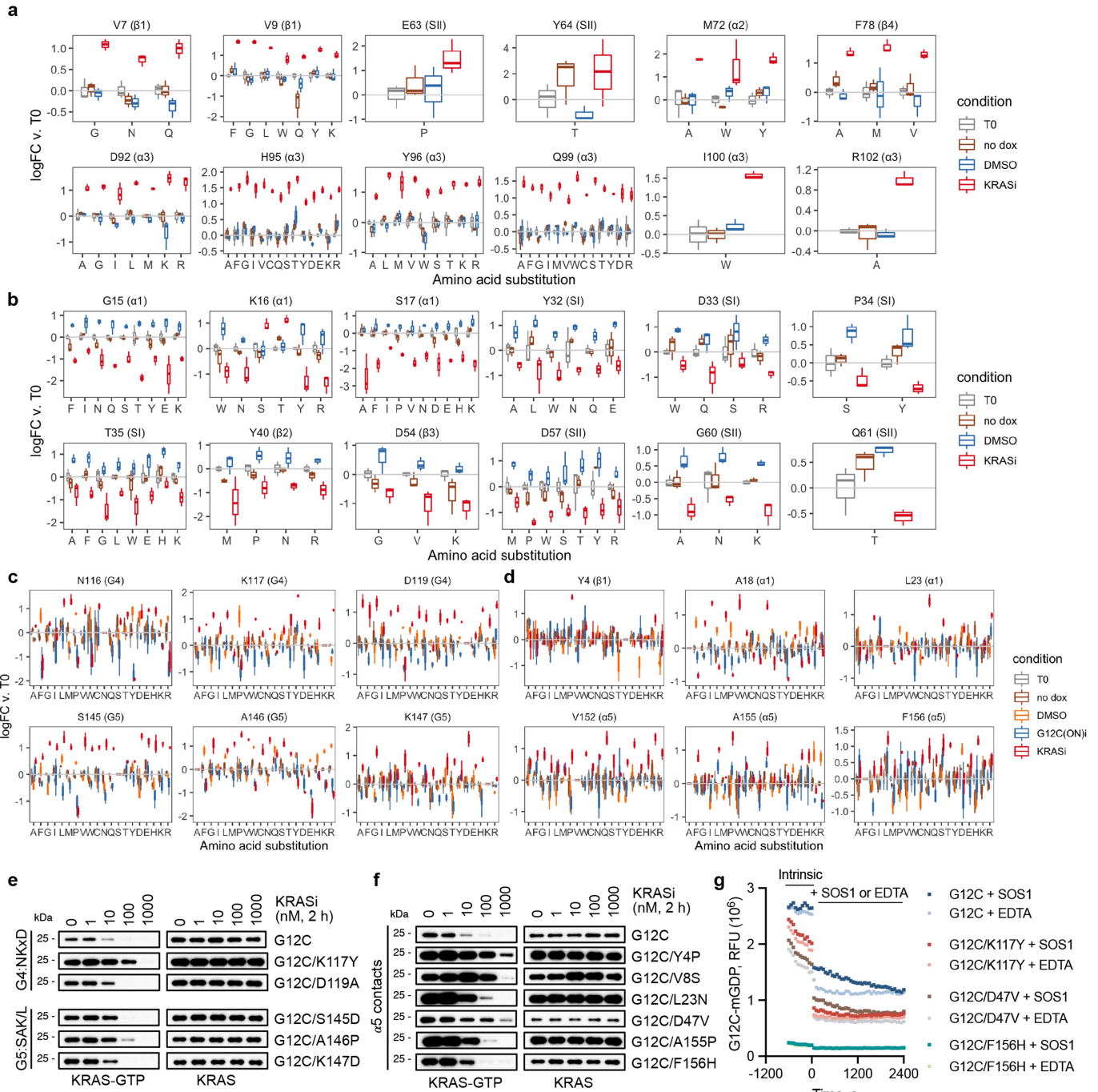
Extended Data Fig. 2 | Biochemical and cellular effects of the KRAS inhibitor. **a,b**, KRAS variants were loaded with GDP or GCP and subjected to isothermal titration calorimetry (ITC) with the KRASi. **c**, The association (on) and dissociation (off) rate constants of drug binding to GDP-loaded KRAS variants (mean \pm s.e.m., $n = 3$). **d**, Effect of KRASi treatment on nucleotide exchange under intrinsic conditions. **e**, KRAS variants were loaded with the non-hydrolyzable GTP analogue GMPPNP (GNP) and reacted with a GST-tagged RBD domain of CRAF. The mixtures were analyzed by GST pull-down and immunoblotting to determine the ability of the drug to displace effectors from the active state of KRAS. Pull-down reactions were analyzed by immunoblotting and quantified by densitometry. **f**, Extracts from HEK293 cells expressing the

indicated variants treated with the KRASi for 2 h were subjected to RBD pull down and immunoblotting. The levels of total and GTP-bound KRAS were quantified by densitometry. **g**, The indicated KRAS variants were loaded with GDP and subjected to ITC in the presence of increasing concentrations of the KRASi. **h**, Effect of KRASi treatment on GTP hydrolysis by KRAS under intrinsic conditions or in the presence of the GAP related domain (GRD) of NF1 (mean \pm s.e.m., $n = 3$). **i**, The indicated KRAS G12C mutant cell lines were treated for 2 h and their extracts were subjected to RBD pull-down and immunoblotting to determine the level of active KRAS. **j**, H2122 cells were treated as shown and analyzed to determine the effect on KRAS activation. A representative of two independent repeats is shown in a, b, d-f, i and j.



Extended Data Fig. 3 | Orthosteric and allosteric effects determine KRAS selectivity. **a**, Extracts from RASless MEFs expressing the indicated RAS isoforms were evaluated by immunoblotting. **b**, HEK293 cells expressing the indicated G12C mutants were treated for 2 h. Cell extracts were subjected to RBD-pull down and immunoblotting to determine the level of active RAS. **c,d**, Effect of isoform mimetic substitutions on RAS inhibition. HEK293 cells

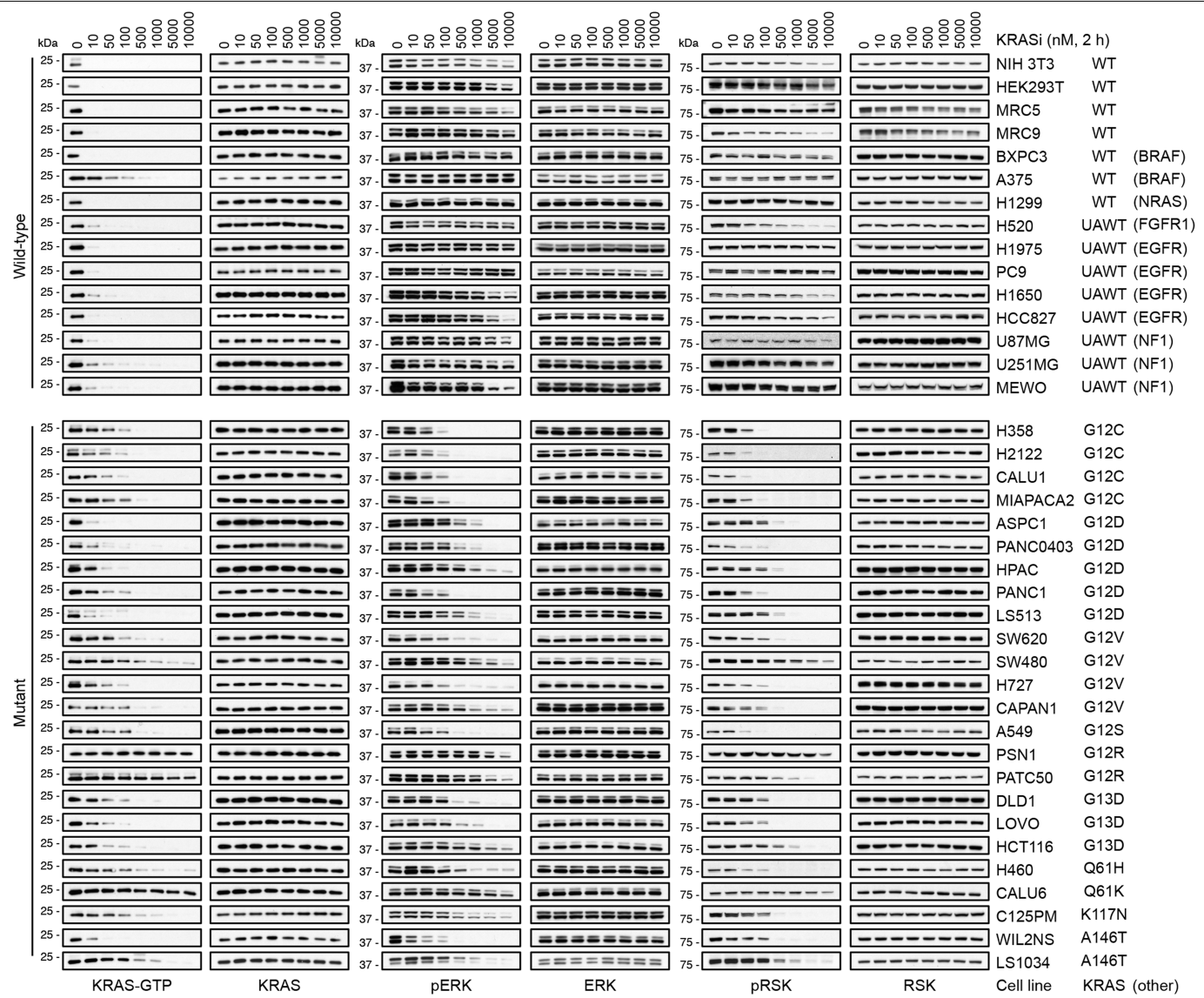
expressing the indicated mutants were treated as shown for 2 h. Cell extracts were subjected to RBD-pull down and immunoblotting to determine the level of active RAS. The effect of H95 mutants is shown in **c** and the effects of P121, S122, N85 and K117 mutants are shown in **c** and **d**. A representative of two independent repeats is shown in **a, b, c** and **d**.



Extended Data Fig. 4 | Saturation mutagenesis screen reveals residues that modulate inhibition. **a,b**, The effect of substitutions in amino acids involved in the drug binding interface (a) or in the RAS-GDP:SOS1 interface (b) are shown ($\text{mean} \pm 95\% \text{CI}$, $n = 3$). Only variants with a $\log \text{FC}$ (KRASI/DMSO) > 1 and $\text{FDR} < 0.05$ are included. All boxplots denote median, interquartile range and Tukey whiskers. **c,d**, As in a, but the cells were treated either with the inactive state selective pan KRASi or with an active state selective KRAS G12C inhibitor. The effect of substitutions in amino acids comprising the G4 and G5 motifs or

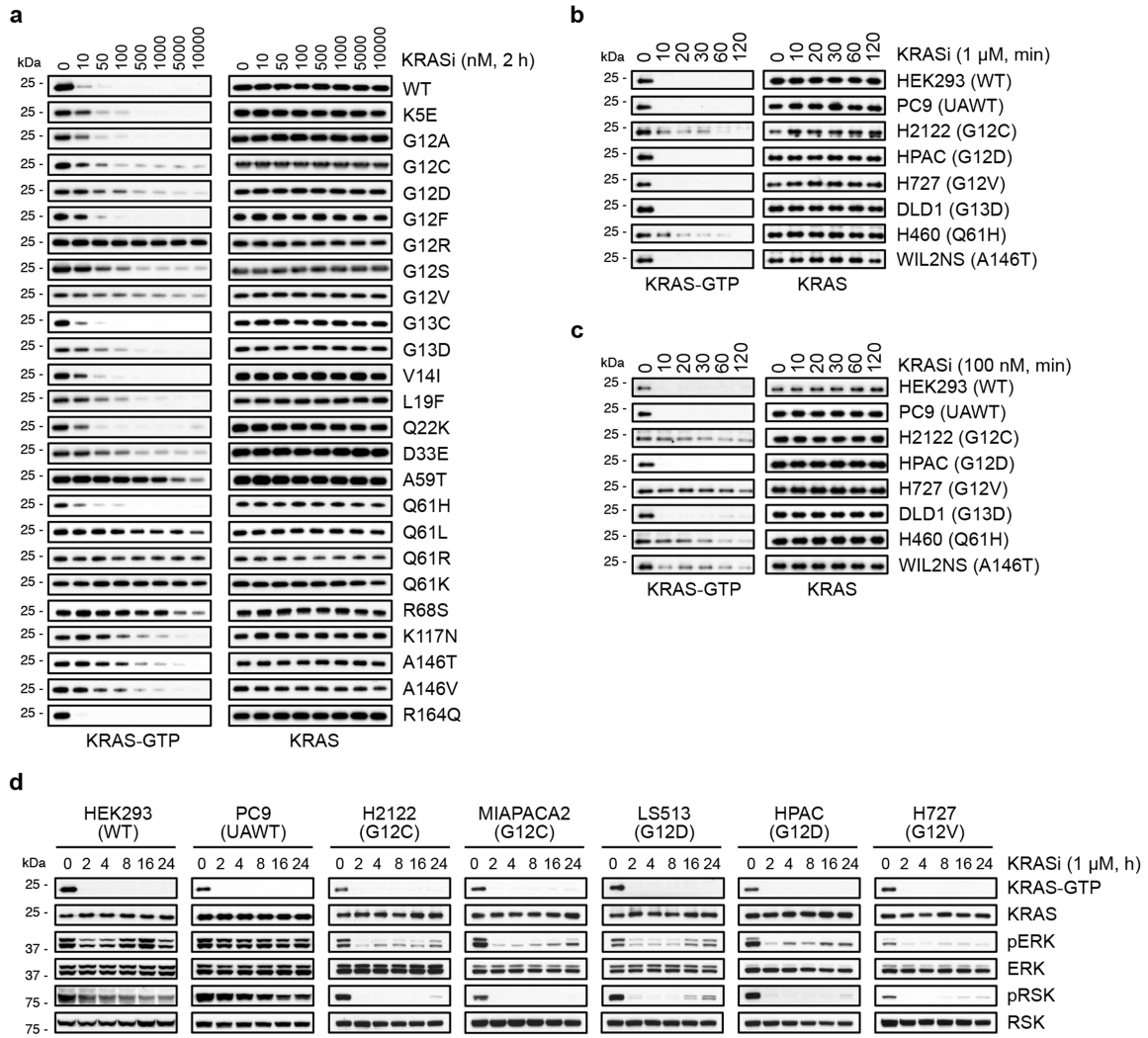
substitutions in amino acids involved in contacts with the $\alpha 5$ helix are shown in c and d, respectively ($\text{mean} \pm 95\% \text{CI}$, $n = 3$). **e,f**, Cell extracts from HEK293 cells expressing the indicated KRAS variants were subjected to RBD-pulldown and immunoblotting to determine the effect on KRAS-GTP. **g**, The indicated KRAS mutants were loaded with mant-GDP and subjected to nucleotide exchange in the absence or the presence of the catalytic subunit of SOS1 or EDTA. A representative of two independent repeats is shown in e, f and g.

Article



Extended Data Fig. 5 | Selective inhibition of oncogenic signaling driven by various KRAS mutants. Extracts from cell lines treated with the KRAS inhibitor were subjected to RBD pull-down and immunoblotting to determine the effect

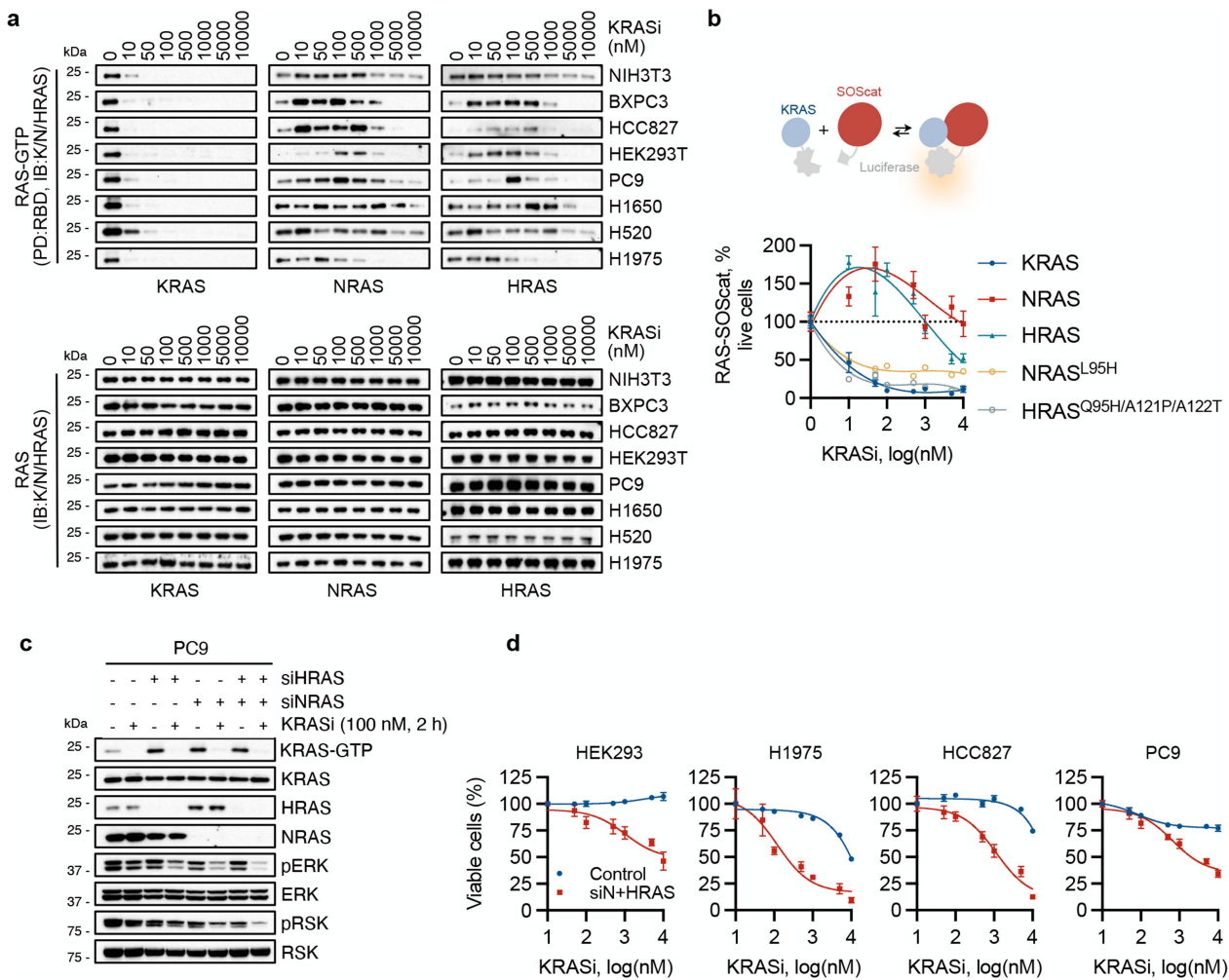
on KRAS and ERK signaling activation. WT: wild-type, UAWT: upstream activated wild-type. Co-occurring alterations in select other genes are shown. The data in Fig. 4a are densitometric quantifications of the immunoblots shown here.



Extended Data Fig. 6 | Rapid and sustained inactivation of common KRAS mutants. **a**, HEK293 cells expressing the indicated KRAS variants were treated as shown and analyzed to determine the effect on KRAS activation. **b-d**, The indicated cell lines were treated over time to determine the effect on KRAS

activation (b-d) and ERK signalling intermediates (d). The cells in b and c were treated in serum-free medium, whereas those in a and d were treated in complete medium. A representative of two independent repeats is shown in a-d.

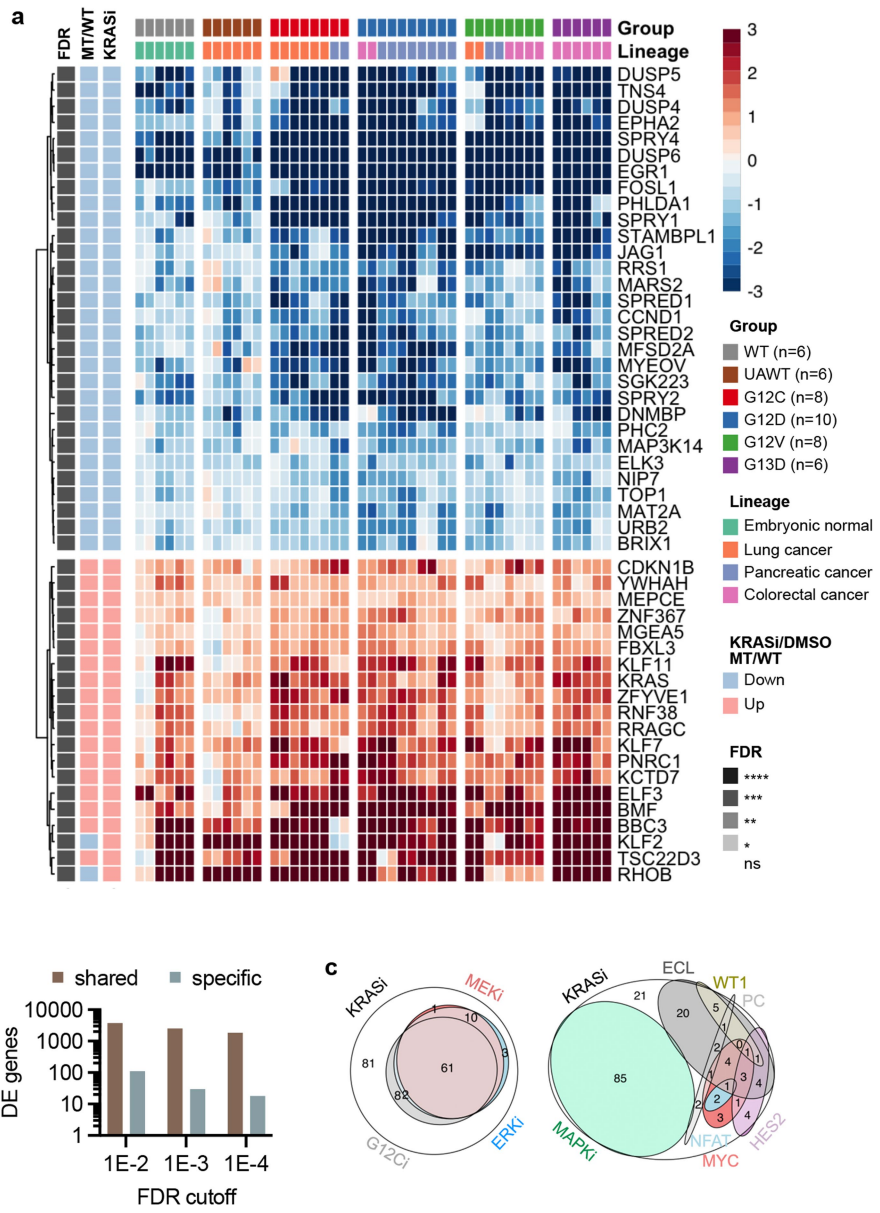
Article



Extended Data Fig. 7 | Drug induced cellular activation of HRAS and NRAS.

a, The indicated KRAS WT cells were treated for 2 h to determine the effect on RAS isoform activation. A representative of two independent repeats is shown. **b**, A split luciferase construct was used to determine the effect of treatment (2 h) on the interaction between RAS variants and the catalytic subunit of SOS1 (SOScat, mean \pm s.e.m., $n = 3$). **c**, The cells were transfected with HRAS- and/or

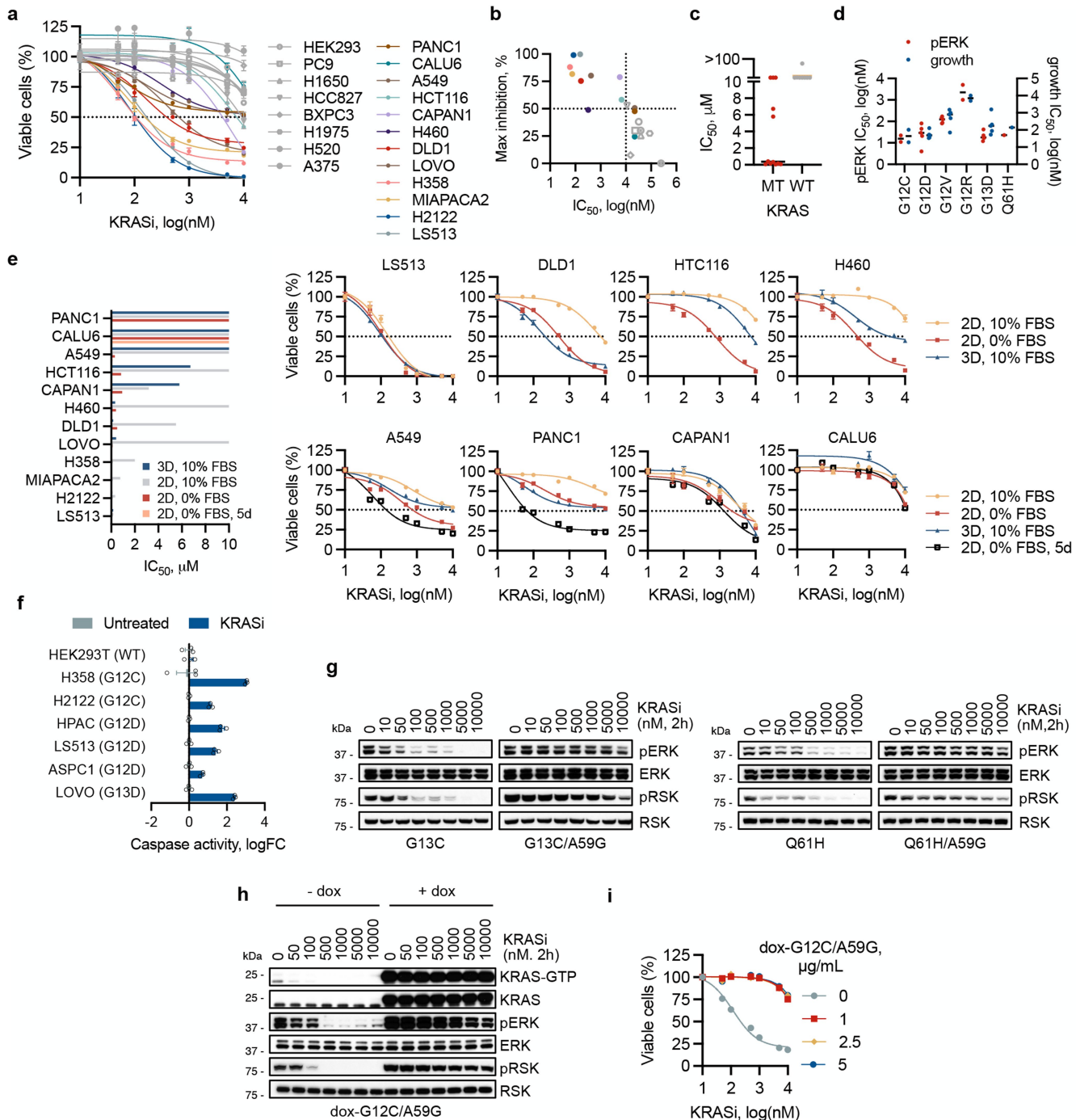
NRAS-specific siRNA pools and treated as shown. Extracts were analyzed to determine the level of KRAS activation and downstream signaling inhibition. A representative of two independent repeats is shown. **d**, The indicated KRAS WT models were transfected with NRAS- and HRAS-specific siRNA pools, followed by treatment with the KRASi for 72 h. The effect on cell viability was determined by the ATP-glow assay (mean \pm s.e.m., $n = 3$).



Extended Data Fig. 8 | Effect of KRASi treatment on transcriptional output. **a**, Differential expression analysis in models with wild-type or mutant KRAS treated for 2 h with the KRASi. The heat map shows the scaled logFC relative to DMSO. Row annotations show the expression trend in the KRASi/DMSO or MT/WT comparisons. The models are grouped as shown. **b**, The number of differentially expressed (DE) genes shared across groups as compared to those

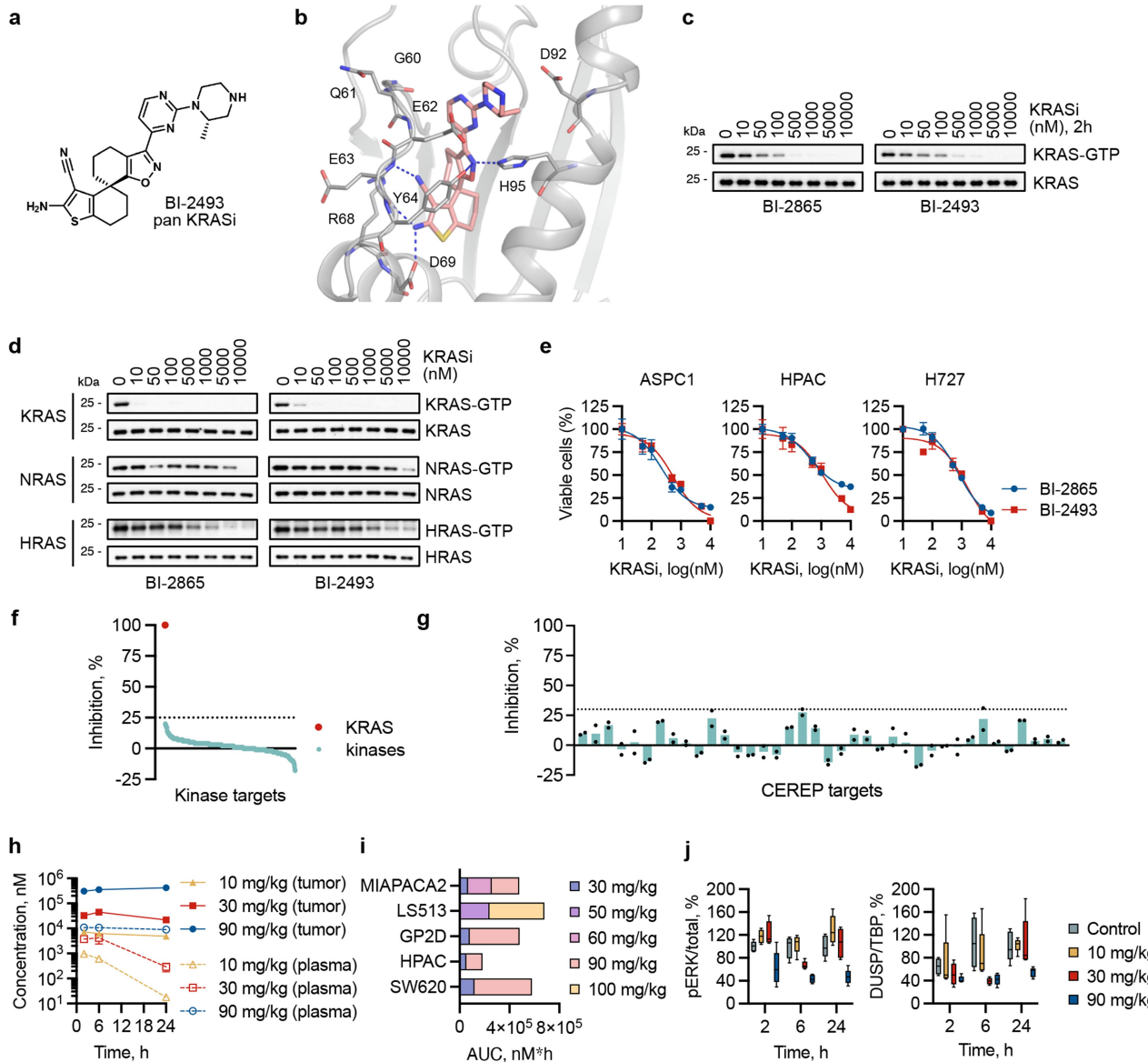
specific for a particular group. **c**, Gene-set enrichment analysis of transcripts down-regulated by treatment. The MAPK-dependent signatures were established experimentally by treating cells with the inhibitors shown (see Methods). The other signatures are from MSigDB. ECL: extracellular ligand; PC: polycomb transcription factors.

Article



Extended Data Fig. 9 | Antiproliferative effect of the KRASi inhibitor. **a–c**, The indicated cells were grown in 3D culture and treated with the KRASi for 72 h and the effect on cell viability (A) was determined using the ATP-glow assay (mean \pm s.e.m., $n = 4$). The effect on maximal inhibition as a function of IC₅₀ (b) and the difference in IC₅₀ between KRAS MT and WT models (c) are shown. **d**, Correlation between ERK and growth inhibition in cell lines with distinct KRAS mutations. **e**, Antiproliferative effect of treatment under the cell culture

conditions shown (mean \pm s.e.m., $n = 4$). **f**, The indicated models were treated for 24 h followed by measurement of caspase activation (mean \pm s.e.m., $n = 3$). **g**, Extracts from HEK293 cells expressing the indicated variants were analyzed to determine the effect of treatment on ERK signaling activation. **h,i**, H358 cells with dox-inducible expression of KRAS G12C/A59G were analyzed as shown to determine the effect on KRAS signaling (h) or proliferation (i, mean \pm s.e.m., $n = 3$). A representative of two independent repeats is shown in g and h.



Extended Data Fig. 10 | Characterization of the *in vivo* pan KRAS inhibitor BI-2493.

a, Chemical structure of BI-2493. **b**, Co-crystal structure of KRAS G13D with BI-2493. **c,d**, CALU1 cells (c) or RASless MEFs expressing the indicated RAS isoforms (d) were treated as shown and analyzed by RBD pulldown and immunoblotting. A representative of two independent repeats is shown. **e**, The indicated cancer cell lines were treated as shown for 72 h. Viable cells were determined by ATP-glow (mean \pm s.e.m., $n = 3$). **f,g**, Effect of KRASi-

treatment ($1\mu\text{M}$) across a panel of 404 kinases (f) or 38 targets commonly used in safety profiling (g). KRAS was not part of the assay and included only as a reference. **h–j**, GP2D (h, i, j) or other (i) xenograft bearing mice were treated with BI-2493 (10–90 mg/kg, p.o. twice a day). Plasma (h, i) or tumors (h, j) from treated mice were used to determine the concentration of BI-2493 or the effect on inhibition of the noted ERK signaling intermediates. **h**: mean \pm s.e.m ($n = 4$), **j**: median, 95% confidence interval and range are shown ($n = 4$).

Article

Extended Data Table 1 | Crystallographic data collection and refinement statistics

Data collection*	KRAS WT precursor 1	KRAS WT BI-2865	KRAS G12C BI-2865	KRAS G12D BI-2865	KRAS G12V BI-2865	KRAS G13D BI-2865	KRAS G13D BI-2493
PDB code	8AZR	8AZV	8AZX	8AZY	8AZZ	8B00	8ONV
Wavelength [Å]	1.54184	1.0000	1.0000	1.0000	0.99982	1.0000	1.0000
Beamline	BRUKER	SLS:X06SA	SLS:X06SA	SLS:X06SA	SLS:X06SA	SLS:X06SA	SLS:X06SA
<i>Data Processing</i>							
Space group	P 2 ₁ 2 ₁ 2	P 21212					
<i>Cell dimensions</i>							
<i>a, b, c</i> (Å)	86.84 40.30 55.89	86.47 40.63 56.17	86.50 40.64 56.02	87.16 40.55 55.94	86.48 40.71 55.99	86.518 40.620 55.979	85.80 40.85 55.96
α, β, γ (°)	90.0 90.0 90.0	90.0 90.0 90.0 90.0 90.0	90.0 90.0 90.0				
Resolution (Å)	55.8-1.6 (1.719-1.604)	47.1-1.0 (1.122-1.047)	56.0-1.0 (1.171-1.042)	36.8-1.1 (1.206-1.094)	56.0-1.0 (1.128-1.025)	56.0-1.0 (1.151-1.037)	56.0-1.0 (1.097-1.011)
Unique Reflections	21248 (1063)	77612 (3882)	56889 (2845)	57094 (2856)	74206 (3711)	65850 (3293)	83260 (4164)
<i>R_{merge}</i>							
CC1/2	1.0 (0.6)	1.0 (0.7)	1.0 (0.7)	1.0 (0.7)	1.0 (0.8)	1.0 (0.8)	1.0 (0.7)
<i>I</i> / σ <i>I</i>	11.4 (1.5)	20.0 (1.6)	17.4 (2.2)	17.7 (1.8)	24.2 (1.9)	18.0 (2.0)	20.3 (1.8)
Completeness (ellipsoidal) (%) **	90.1 (45.4)	94.7 (58.2)	94.6 (68.3)	94.9 (75.8)	94.5 (62.6)	94.7 (69.2)	93.1 (49.2)
Completeness (spherical) (%)	80.4 (21.9)	82.6 (22.2)	59 (10.3)	69.1 (13.8)	74.3 (15.0)	68.5 (12.9)	80.6 (18.9)
Redundancy	4.7 (2.1)	12.1 (7.5)	12.3 (9.6)	12.2 (10.3)	12.1 (6.0)	10.9 (6.9)	11.8 (5.6)
<i>Refinement***</i>							
<i>R_{work}</i> / <i>R_{free}</i>	17.9 / 23.2	15.5 / 17.4	16.1 / 19.7	16.4 / 19.7	14.5 / 16.5	14.4 / 16.1	13.4 / 15.7
<i>No. atoms (excl. hydrogens)</i>							
Protein	1372	1450	1412	1412	1430	1384	1428
Ligands/ion	32	33	33	33	33	33	33
Water	303	262	248	220	281	247	281
<i>B-factors</i>							
Protein	14.4	18.2	18.5	18.1	19.3	18.1	16.6
Ligands	12..4	20.5	19.7	25.8	22.2	21.1	15,2
Water	26.7	34.7	36.6	35.4	39.9	37.4	38.3
<i>R.m.s. deviations</i>							
Bond lengths(Å)/ angles (°)	0.008/ 0.98	0.09 / 0.084	0.09 / 1.15	0.010 / 1.05	0.084 / 1.10	0.09 / 1.15	0.008 /1.11

* Values in parentheses are for highest-resolution shell.

** Data were scaled anisotropically with Staraniso.

*** Value output by Phenix

Reporting Summary

Nature Portfolio wishes to improve the reproducibility of the work that we publish. This form provides structure for consistency and transparency in reporting. For further information on Nature Portfolio policies, see our [Editorial Policies](#) and the [Editorial Policy Checklist](#).

Statistics

For all statistical analyses, confirm that the following items are present in the figure legend, table legend, main text, or Methods section.

n/a Confirmed

- The exact sample size (n) for each experimental group/condition, given as a discrete number and unit of measurement
- A statement on whether measurements were taken from distinct samples or whether the same sample was measured repeatedly
- The statistical test(s) used AND whether they are one- or two-sided
Only common tests should be described solely by name; describe more complex techniques in the Methods section.
- A description of all covariates tested
- A description of any assumptions or corrections, such as tests of normality and adjustment for multiple comparisons
- A full description of the statistical parameters including central tendency (e.g. means) or other basic estimates (e.g. regression coefficient) AND variation (e.g. standard deviation) or associated estimates of uncertainty (e.g. confidence intervals)
- For null hypothesis testing, the test statistic (e.g. F , t , r) with confidence intervals, effect sizes, degrees of freedom and P value noted
Give P values as exact values whenever suitable.
- For Bayesian analysis, information on the choice of priors and Markov chain Monte Carlo settings
- For hierarchical and complex designs, identification of the appropriate level for tests and full reporting of outcomes
- Estimates of effect sizes (e.g. Cohen's d , Pearson's r), indicating how they were calculated

Our web collection on [statistics for biologists](#) contains articles on many of the points above.

Software and code

Policy information about [availability of computer code](#)

Data collection	For Saturation mutagenesis, PCR products were subjected to Hiseq analysis at 2x150 bp. Bulk sequencing was carried out on HiSeq in a 2X 150bp paired end run with an average of 30 million paired reads per sample. The diffraction data was collected at X06SA beamline of the Swiss Light Source (Paul Scherrer Institute).
Data analysis	For saturation mutagenesis, count files were generated by using the ORFcall software and the raw read counts of each treatment groups were analyzed using edgeR to determine changes. For bulk sequencing results were aligned to GRCh38 using HISAT2 and transcripts were counted using HTSeq in Python. The count data matrix was then processed by using limma and edgeR in R/Bioconductor. The diffracted images were processed with autoPROC34 and all structures were solved by molecular replacement using a previously solved structure. Model building and refinement was performed with standard protocols using CCP4, COOT, autoBUSTER v.2.11.2 (http://www.globalphasing.com) and Phenix35,36. For westernblot analysis, ImageJ was used.

For manuscripts utilizing custom algorithms or software that are central to the research but not yet described in published literature, software must be made available to editors and reviewers. We strongly encourage code deposition in a community repository (e.g. GitHub). See the Nature Portfolio [guidelines for submitting code & software](#) for further information.

Data

Policy information about [availability of data](#)

All manuscripts must include a [data availability statement](#). This statement should provide the following information, where applicable:

- Accession codes, unique identifiers, or web links for publicly available datasets
- A description of any restrictions on data availability
- For clinical datasets or third party data, please ensure that the statement adheres to our [policy](#)

The data availability statement has been updated (in text and reporting forms). The data has been deposited in appropriate repositories.

The pan KRAS inhibitors ("GDP-KRAS inhibitors") are available as part of a collaborative program via Boehringer Ingelheim's open innovation portal opnMe.com: <https://opnme.com/collaborate-now/GDP-KRAS-inhibitor-bi-2493>.

The co-crystal structures have been deposited in the PDB with accession codes: 8AZR, 8AZV, 8AZX, 8AZY, 8AZZ and 8B00.

The RNAseq results have been deposited in NCBI Geo with accession number: GSE228010

All other data are available upon request.

Human research participants

Policy information about [studies involving human research participants](#) and [Sex and Gender in Research](#).

Reporting on sex and gender No human subjects were used in this study.

Population characteristics No human subjects were used in this study.

Recruitment No human subjects were used in this study.

Ethics oversight No human subjects were used in this study.

Note that full information on the approval of the study protocol must also be provided in the manuscript.

Field-specific reporting

Please select the one below that is the best fit for your research. If you are not sure, read the appropriate sections before making your selection.

Life sciences Behavioural & social sciences Ecological, evolutionary & environmental sciences

For a reference copy of the document with all sections, see nature.com/documents/nr-reporting-summary-flat.pdf

Life sciences study design

All studies must disclose on these points even when the disclosure is negative.

Sample size Varies across experiments. Please see methods section for more details.

Data exclusions All data were used in statistical testing, unless otherwise specified in the text.

Replication The experimental replicates are stated in the figure legends. All stated replicates indicate biological replicates.

Randomization In vivo tumor growth experiments: mice were treated in a random manner with either vehicle or drug

Blinding Tumor growth measurements were carried out in a blinded manner by a technician who was not aware of the goals of the experiment.

Reporting for specific materials, systems and methods

We require information from authors about some types of materials, experimental systems and methods used in many studies. Here, indicate whether each material, system or method listed is relevant to your study. If you are not sure if a list item applies to your research, read the appropriate section before selecting a response.

Materials & experimental systems

n/a	Involved in the study
<input type="checkbox"/>	<input checked="" type="checkbox"/> Antibodies
<input type="checkbox"/>	<input checked="" type="checkbox"/> Eukaryotic cell lines
<input checked="" type="checkbox"/>	<input type="checkbox"/> Palaeontology and archaeology
<input type="checkbox"/>	<input checked="" type="checkbox"/> Animals and other organisms
<input checked="" type="checkbox"/>	<input type="checkbox"/> Clinical data
<input checked="" type="checkbox"/>	<input type="checkbox"/> Dual use research of concern

Methods

n/a	Involved in the study
<input checked="" type="checkbox"/>	<input type="checkbox"/> ChIP-seq
<input checked="" type="checkbox"/>	<input type="checkbox"/> Flow cytometry
<input checked="" type="checkbox"/>	<input type="checkbox"/> MRI-based neuroimaging

Antibodies

Antibodies used

Primary (1:1000 dilution, otherwise stated): Pan-Ras (1862335, Thermo), KRAS (WH0003845M1, sigma), HRAS(18295-1-AP, Proteintech. 1:300 dilution), NRAS (SC-31, santa cruz, 1:300 dilution)), FLAG M2(F1084, sigma,) HA (2367S, CST), GST (SC-138, santa cruz,) HIS tag (2365S, CST), ERK (4696S, CST), pERK (9101L, CST), pRSK(8753S, CST), RSK1/RSK2/RSK3(9355S, CST) Secondary (1:3000 dilution): Mouse IgG HRP (7076S, CST), Rabbit IgG HRP (A4914, sigma)

Validation

We have validated the antibodies for pan-RAS, KRAS, HRAS and NRAS in this study by using siRNA targeting specific forms of RAS as well as using a 'RASless' cell lines that express only 1 form of RAS. All other antibodies have been validated in our previous publications. (Xue et al., Nature 2020, Zhao et al., Nature 2021 and Li et al., Science 2021)

Eukaryotic cell lines

Policy information about [cell lines and Sex and Gender in Research](#)

Cell line source(s)

ATCC: NIH/3T3 HEK283T, MRC5, MRC9, BXPC3, A375, H1299, H520, H1975, PC9, H1650, HCC827, U87MG, MEWO, H358, H2122, CALU1, MIAPACA2, ASPC1, PANCO403, HPAC, PANC1, LS513, SW620, SW480, H727, CAPAN1, A549, PSN1, PATC50, DLD1, LOVO, HCT116, H460, CALU6, WIL2NS, LS1034
Sigma: PC9, C125pm. Kerafast:U251MG, Accegen :BA/F3

Authentication

Cell lines were directly obtained from the vendor before use and studies were carried out before 20 passages upon purchase. Also cell lines were authenticated by MSK IMPACT sequencing to confirm the KRAS mutations. Cell lines bearing KRAS G12C mutation were also confirmed by testing with KRAS G12C specific inhibitors.

Mycoplasma contamination

The cell line used in the study were tested negative for mycoplasma.

Commonly misidentified lines (See [ICLAC register](#))

No commonly misidentified cell lines were used in the study.

Animals and other research organisms

Policy information about [studies involving animals; ARRIVE guidelines](#) recommended for reporting animal research, and [Sex and Gender in Research](#)

Laboratory animals

Athymic or NSG mice were used as indicated in the methods.

Wild animals

No wild animals were used in the study.

Reporting on sex

7-8 week old female nude mice were used for the study.

Field-collected samples

No field collected samples were used in the study.

Ethics oversight

Mice were housed according to the internal institutional and Austrian governmental and European Union guidelines (Austrian Animal Protection Laws, ETS-123) at Bl or according to the Institutional Animal Care and Use Committee (IACUC) guidelines at MSKCC. All animal studies were approved by the internal ethics and the local governmental committee.

Note that full information on the approval of the study protocol must also be provided in the manuscript.